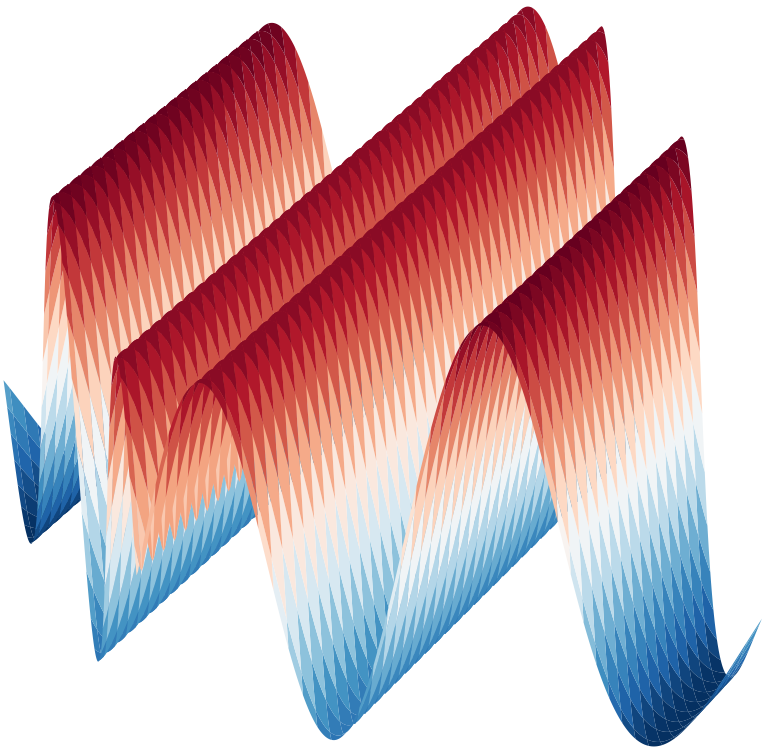

Eigenvector continuation and strongly interacting cold atom systems

Predicted evolution of the energy spectrum as a function of the tunable interaction strength between trapped ultracold atoms

Master's thesis in Physics

CARL EKLIND

DEPARTMENT OF PHYSICS

CHALMERS UNIVERSITY OF TECHNOLOGY
Gothenburg, Sweden 2021
www.chalmers.se

Master's thesis 2021

Eigenvector continuation and strongly interacting cold atom systems

Predicted evolution of the energy spectrum as a function of the tunable interaction strength between trapped ultracold atoms

Carl Eklind

CHALMERS
UNIVERSITY OF TECHNOLOGY

Department of Physics
Division of Subatomic, High Energy and Plasma Physics
Chalmers University of Technology
Gothenburg, Sweden 2021

Eigenvector continuation and strongly interacting cold atom systems
Predicted evolution of the energy spectrum as a function of the tunable interaction strength between trapped ultracold atoms
Carl Eklind

Supervisor: Christian Forssén, Department of Physics
Examiner: Christian Forssén, Department of Physics

Master's Thesis 2021
Department of Physics
Division of Subatomic, High Energy and Plasma Physics
Chalmers University of Technology
SE-412 96 Gothenburg
Telephone: +46 31 772 1000

Cover: Wave function of the fourth excited state in position coordinates for two ultracold atoms. The atoms are trapped in an external harmonic oscillator trap and interact with a zero-range interaction of strength $g = 100\,\ell\hbar\omega$. The eigenstates are used as training data for the *Eigenvector continuation* emulator.

Typeset in LaTeX
Printed by Chalmers Reproservice
Gothenburg, Sweden 2021

Abstract

New experimental techniques have made it possible to trap and cool atoms to extremely low temperatures, which have initiated a new research field—the study of ultracold atoms. In this thesis, we consider one-dimensional many-body quantum systems of ultracold atoms with a zero-range interaction. The atoms are trapped in a tightly confining harmonic oscillator potential and the resulting Hamiltonian depends linearly on the tunable interaction strength. The aim of this study is to describe the evolution of the energy spectrum as a function of the interaction strength by exploiting *eigenvector continuation*—a recently developed method that has been proposed as a very efficient and accurate emulator for solving quantum many-body problems. Emulation is achieved by utilizing a limited set of calculated eigenvectors as training data to construct subspace-projected Hamiltonian matrices that can be used to approximately extrapolate the smooth eigenvector trajectory in the full Hilbert space. In this study, we show that the method of eigenvector continuation is very efficient and provides accurate predictions of the energy spectrum for both attractive and repulsive interaction strengths with just a few training vectors. The method performs extremely well for the two-particle system, where the training vectors correspond to wave functions in a relative coordinate basis, but also for the many-particle system with a basis constructed from single-particle states. In addition, we perform an extensive analysis regarding the performance of the emulator and its dependence on the choice of training data. As a result, we propose an algorithm for finding the optimal set of training data and measure the emulator performance using K-fold cross validation.

Keywords: eigenvector continuation, exact diagonalization ultracold atoms, Busch model.

Acknowledgements

I want to thank my supervisor Christian Forssén for his enthusiastic support and valuable advice during my Master's thesis project. I would also like to thank Håkan Johansson for his technical support regarding the use of the computers at the research group *Theoretical Subatomic Physics*.

Carl Eklind, Gothenburg, June 2021

Table of Contents

1 Introduction **1**
- 1.1 Background . . . 1
- 1.2 Aim of the study . . . 2
- 1.3 Structure of the thesis . . . 2

2 Ultracold atoms **5**
- 2.1 One-dimensional system of two cold atoms . . . 5
  - 2.1.1 The harmonic oscillator basis . . . 6
  - 2.1.2 Analytical solution to the Busch model . . . 7
  - 2.1.3 Numerical solution . . . 11
- 2.2 Generalized many-body system . . . 14

3 Eigenvector continuation **17**
- 3.1 Purpose of using an emulator . . . 17
- 3.2 Theory and implementation . . . 17
  - 3.2.1 Efficiency of an EVC emulator . . . 20
  - 3.2.2 Mathematical motivation of eigenvector continuation . . . 20
  - 3.2.3 Limitations when constructing an EVC emulator . . . 20
  - 3.2.4 Generalization with more parameters . . . 21

4 Two-body energy emulations **23**
- 4.1 Energy spectrum emulations . . . 23
  - 4.1.1 Predictions of the ground state energy . . . 24
  - 4.1.2 Predictions of the excited state energy . . . 31
- 4.2 Optimal training vector algorithm . . . 34

5 Many-body energy emulations **39**

6 Conclusion and outlook **43**

References **47**

1. Introduction

The recently developed method of *eigenvector continuation* (EVC) [1] has been proposed as a very efficient and accurate emulator for solving quantum many-body problems [2]. The emulations rely on utilizing a limited set of calculated eigenvectors as training data to construct subspace-projected Hamiltonian matrices. This subspace projection can be used to approximately extrapolate the smooth eigenvector trajectory in the full Hilbert space as some continuous parameter in the Hamiltonian is varied. The emulators can be used to predict the eigenvalue and other observables for a quantum system and have previously been used to construct emulators mainly within the field of nuclear physics [2]–[4].

This study applies the method of eigenvector continuation for the first time to a quantum system within the field of *ultracold atoms*. In particular, we consider simple but realistic one-dimensional systems of atoms in a harmonic oscillator trap with a tunable interaction strength. For two distinguishable atoms, with a zero-range interaction, there is a known analytical solution [5] while for more than two particles there are numerical solutions based on exact diagonalization [6]. It is our aim to construct emulators that mimic these full solutions as a function of the interaction strength at a very small computational cost.

1.1 Background

The method of EVC was introduced in the end of 2017 [1] as a new technique for approximating eigenvalues and eigenvectors of Hamiltonian matrices for quantum many-body systems. Such matrices often become very large, and eigenvector continuation was used to solve the Schrödinger equation for parameters in the Hamiltonian beyond some threshold values, where more conventional approximation methods based on perturbation theory have failed.

In 2019, EVC was proposed as an emulator for predicting nuclear many-body observables [2]. The EVC emulators are constructed using full solutions as training data, making it a machine-learning approach. The method of eigenvector continuation and its use as an emulator has been studied ever since and due to its extreme efficiency, it broadens the possibilities of calculations within quantum many-body theory. *Chalmers University of Technology* is one of the universities that drive the development and usage of EVC emulators for atomic nuclei calculations [2]–[4], [7]. Here we broaden these efforts to incorporate studies of ultracold atoms.

New experimental methods have made it possible to trap and cool atoms to extremely low temperatures, close to the absolute zero. The 1997 Nobel Prize in Physics was awarded to the development of techniques using laser light to trap and cool atoms [8]. This new method, together with *evaporative cooling* [9], led to the experimental realization of Bose-Einstein condensation in 1995 [10]. This phenomenon, originally predicted by Albert Einstein, occurs when a gas of bosonic

atoms is cooled down to extremely low temperatures making the ground state macroscopically occupied. The achievements of Bose-Einstein condensation were also awarded with the Nobel Prize in Physics, just four years later, in 2001 [11]. This was the foundation for the new field of *ultracold atoms*, which has been continuously growing, ever since.

The study of ultracold atoms is associated with the possibility for immense experimental control. The shape of the trap, as well as the numbers and kinds of atoms can be varied. Furthermore, the interatomic interaction strength can be tuned by exploiting the technique of Feshbach resonances [12]. This experimental control in the study of ultracold atomic gases enables the investigation of multiple phenomena in quantum physics, e.g. the behavior of many-body quantum mechanical systems in different interaction regimes—from weak to strong coupling. This project will treat one-dimensional many-body quantum systems with a zero-range interaction, which appear in the study of ultracold atoms in a tightly confining harmonic oscillator trap.

1.2 Aim of the study

The aim of this study is to describe the evolution of the energy spectrum as a function of the tunable interaction strength by utilizing the recently developed method of *eigenvector continuation*. In order to achieve this, we first need to find full solutions to the ultracold atomic quantum system for some selected values of the interaction strength by constructing Hamiltonian matrices and solving the Schrödinger equation numerically using exact diagonalization (ED). To analyze the performance of the emulators, we also want to calculate the energy eigenvalues and eigenvectors for a wider range of interaction strengths.

In this work we apply EVC for the first time to systems of ultracold atoms. Therefore, the main intention is to show that EVC emulators can predict the energy spectrum as a function of the tunable interaction strength—in both the attractive and repulsive regime—for one-dimensional systems of ultracold atoms in a harmonic oscillator trap. We also aim to investigate the accuracy and efficiency of the constructed emulators, as well as the choice of optimal training data.

1.3 Structure of the thesis

The thesis is divided into the following chapters: *Ultracold atoms*, *Eigenvector continuation*, *Two-body energy emulations*, *Many-body energy emulations* and *Conclusion and outlook*.

In the next chapter, *Ultracold atoms*, we present the systems that will be studied, with an analytical derivation of the energy spectrum for two interacting distinguishable atoms in a one-dimensional trap [5]. Furthermore, we also present the analytical expressions for the Hamiltonian matrix elements, and numerically find eigenvalues and eigenvectors with exact diagonalization in `Python` using methods from `NumPy` [13] and `SciPy` [14]. These eigenvectors will later be used as training

data for the EVC emulators. For the many-body systems, we instead use a code, written in `C++`, by *J. Lindgren* [6], [15] to obtain the Hamiltonian matrices.

The theory and implementation of EVC is presented in the third chapter—*Eigenvector continuation*. The emulated evolution of the energy spectrum is presented in the two result chapters: *Two-body energy emulations* and *Many-body energy emulations*. The first one includes the emulator results for the two-body system, where we also propose an algorithm for finding the optimal training vectors for constructing the most accurate EVC emulators. In the many-body results we present the energy emulations of the many-body systems with $2 + 1$ and $4 + 1$ ultracold atoms.

Finally, in *Discussion and conclusion*, we discuss how the proposed algorithm could be used in practice and provide a more in-depth interpretation of the result. In addition, we also discuss how the system could be further generalized with multiple interaction parameters as well as with a more realistic short-range interaction. This would result in additional continuous parameters in the model, yielding more complex emulations.

2. Ultracold atoms

In this chapter, the theory of the ultracold atomic system is described. We consider one-dimensional many-body quantum systems of ultracold atoms with a zero-range interaction. The atoms are trapped in a tightly confining harmonic oscillator potential and the resulting Hamiltonian depends linearly on the tunable interaction strength g. The system can be experimentally realized, where the atoms are first cooled using *laser cooling* [16] followed by *evaporate cooling* [9] to reach the ultracold regime of µK or nK. Furthermore, the harmonic oscillator trap is accomplished using *standing-wave laser fields*, with the ability to produce optical lattices of one, two or three dimensions. The interatom interaction, however, can be arbitrarily tuned by utilizing the so-called *Feshbach resonance* [12]. The ultracold atomic systems consider in this project have been experimentally realized using Lithium atoms [17] and Sodium atoms [18].

The aim of this study is to describe the evolution of the energy spectrum as a function of g by exploiting *eigenvector continuation* [1]. Emulation is achieved by utilizing a limited set of calculated eigenvectors as training data. Therefore, we need to solve the Schrödinger equation numerically to obtain the energy eigenvalues with corresponding eigenvectors. Therefore, we need to find expressions for the Hamiltonian matrix elements. In addition, there is an analytical expression for the energies of two-atomic system [5], where the derivation will be presented.

2.1 One-dimensional system of two cold atoms

The one dimensional two-body system considered in this work consists of two distinguishable atoms, denoted 1 and 2, in a harmonic oscillator trap with a zero-range interaction having a tunable strength. The single dimension of the system is realized by a tightly confining harmonic oscillator trap, where the atoms are only allowed to move in one direction. The kinetic energy of the two particles and the potential energy due to the harmonic oscillator trap are described by a simple one-dimensional harmonic oscillator Hamiltonian. Furthermore, the zero range interaction is expressed as a product of the interaction strength g and the Dirac delta function $\delta(x_1 - x_2)$, hence yielding a contribution only when the atoms are located at the same position, i.e. when $x_1 = x_2$. The total Hamiltonian of the system, thus becomes

$$\mathcal{H}_{\text{tot}} = \frac{p_1^2}{2m_1} + \frac{p_2^2}{2m_2} + m_1\omega\,\frac{x_1^2}{2} + m_2\omega\,\frac{x_2^2}{2} + g\delta(x_1 - x_2), \tag{2.1}$$

where $p_{1,2}$ $x_{1,2}$ are the momentum and position operators for atom 1 and 2, respectively. Note that the unit of the interaction strength is energy times length[1].

[1] Remember that the delta function $\delta(x)$ has unit reciprocal length, since the integral over x is dimensionless.

Since the interaction only depends on the relative position, we want to separate the Hamiltonian by introducing relative (Rel.) and center of mass (CM) coordinates, i.e.

$$\begin{aligned} &\text{Rel:} \quad x = x_1 - x_2, && p = \frac{m_2 p_1 - m_1 p_2}{m_1 + m_2}, && \mu = \frac{m_1 m_2}{m_1 + m_2}, \\ &\text{CM:} \quad X = \frac{m_1 x_1 + m_2 x_2}{m_1 + m_2}, && P = p_1 + p_2, && M = m_1 + m_2. \end{aligned} \tag{2.2}$$

Note that this transformation conserves the canonical commutation relations, i.e. $[x, p] = [X, P] = \mathrm{i}\hbar$. Using this transformation, we obtain

$$\mathcal{H}_{\text{tot}} = \underbrace{\frac{p^2}{2\mu} + \mu\omega\frac{x^2}{2} + g\delta(x)}_{\equiv\mathcal{H}} + \underbrace{\frac{P^2}{2M} + M\omega\frac{X^2}{2}}_{\equiv\mathcal{H}_{\text{CM}}} \equiv \mathcal{H} + \mathcal{H}_{\text{CM}}. \tag{2.3}$$

where the total Hamiltonian is split into two separate Hamiltonians expressed in relative and CM coordinates, respectively. The solution of the Schrödinger equation for the total system can therefore be separated. The total wave function ψ_{tot} will factorize into $\psi_{\text{tot}} = \psi_{\text{rel}} \otimes \psi_{\text{cm}}$ and the total energy can be expressed as the sum of the relative and CM energy, $E_{\text{tot}} = E + E_{\text{CM}}$. The CM Hamiltonian does not include any interaction, making its solutions trivial. Hence, in this study, we are only interested in the Hamiltonian in relative coordinates, namely

$$\mathcal{H} = \frac{p^2}{2\mu} + \mu\omega\frac{x^2}{2} + g\delta(x) \equiv \mathcal{H}(g), \tag{2.4}$$

which is known as the Busch model [5]. The stationary states of the relative motion between the ultracold atoms are described by the time-independent Schrödinger equation

$$\mathcal{H}\left|\psi\right\rangle = E\left|\psi\right\rangle, \tag{2.5}$$

where $|\psi\rangle$ denotes the stationary energy eigenstates of the two-atomic system with the corresponding energy eigenvalue E. Notice that $\mathcal{H}$ is linearly dependent on the interaction strength g, thus solving the Schrödinger equation yields a continuous energy dependence in g, i.e. $E(g)$. However, it is important to note that $E(g)$ is not linear in g, unless it would have been a perturbed interaction.

2.1.1 The harmonic oscillator basis

We notice that the left part of the Hamiltonian $\mathcal{H}$ in (2.4) is the simple one-dimensional harmonic oscillator Hamiltonian in relative coordinates, and thus with the reduced mass μ. It describes the kinetic energy in relative coordinates of the two ultracold atoms, as well as the potential energy induced by the harmonic oscillator trap. This Hamiltonian is here denoted H_0, i.e.

$$H_0 \equiv \frac{p^2}{2\mu} + \mu\omega\frac{x^2}{2}. \tag{2.6}$$

The solutions to the time-independent Schrödinger equation of the simple harmonic oscillator H_0 are well known and they satisfy

$$H_0 \left|n\right\rangle = E_n \left|n\right\rangle, \qquad E_n = \left(n + \frac{1}{2}\right)\hbar\omega, \qquad n \in \mathbb{N}, \tag{2.7}$$

where $|n\rangle$ is known as the *number state* or *Fock state*. The infinite set of eigenstates to H_0, $\{|n\rangle\}_{n=0}^{\infty}$ form a complete and orthonormal basis, namely

$$\langle n|n'\rangle = \delta_{nn'}, \qquad \sum_{n=0}^{\infty} |n\rangle\langle n| = \mathbb{1}. \tag{2.8}$$

The eigenstates of H_0 in the position basis, i.e. the *wave functions* $\psi_n(x)$ are obtained as the overlap integral and have the known closed formed expressions

$$\psi_n(x) \equiv \langle x|n\rangle = \frac{1}{\sqrt{2^n\, n!}} \left(\frac{\mu\omega}{\pi\hbar}\right)^{1/4} \mathrm{e}^{-\mu\omega x^2/2\hbar}\, H_n\left(\sqrt{\frac{\mu\omega}{\hbar}}\, x\right), \tag{2.9}$$

where $H_n(x)$ are the so-called *Hermite polynomials* [19, Ch. 2.3]. The characteristic length scale of the harmonic oscillator, also known as the *oscillator length*, is

$$\ell = \sqrt{\frac{\hbar}{\mu\omega}}, \tag{2.10}$$

while the characteristic energy scale is $\hbar\omega$. Therefore, these natural units will be used to express length and energy, respectively, all through this study. The expression for the position wave function in (2.9) can be simplified by introducing the dimensionless relative position $\xi \equiv x/\ell$, such that

$$\psi_n(\xi) = \frac{1}{\sqrt{\ell}} \frac{\mathrm{e}^{-\xi^2/2} H_n(\xi)}{\pi^{1/4}\sqrt{2^n\, n!}}, \tag{2.11}$$

We also introduce the dimensionless energies e and $e_n = n + \frac{1}{2}$, as well as the dimensionless interaction strength $\tilde{g}$ by defining

$$E \equiv e\hbar\omega, \qquad E_n \equiv e_n\hbar\omega, \qquad g \equiv \tilde{g}\,\ell\hbar\omega. \tag{2.12}$$

Furthermore, we introduce the interaction Hamiltonian H_1 that corresponds to the zero-range interaction term in (2.4) with $\tilde{g} = 1$

$$H_1 \equiv \ell\hbar\omega\, \delta(x), \tag{2.13}$$

and using this, the Hamiltonian of the two ultracold distinguishable atoms in relative coordinates becomes

$$\mathcal{H} = H_0 + \tilde{g}H_1 \equiv \mathcal{H}(\tilde{g}). \tag{2.14}$$

Hence, the time-independent Schrödinger equation can now be written as

$$(H_0 + \tilde{g}H_1)\left|\psi\right\rangle = e\hbar\omega \left|\psi\right\rangle. \tag{2.15}$$

2.1.2 Analytical solution to the Busch model

The Hamiltonian in (2.4) is one of the few quantum systems that has an analytical solution [5] and the derivation of an analytical expression for e in (2.15) will be presented[2]. To find the analytical expressions for the dimensionless energy e in the

[2] Inspired by the original derivation in [5], and also the derivation in [15].

time-independent Schrödinger equation (2.15), one starts by multiplying with $\langle n|$ from the left. This yields

$$e\hbar\omega \langle n|\psi\rangle = \langle n|H_0|\psi\rangle + \tilde{g}\langle n|H_1|\psi\rangle = e_n\hbar\omega\langle n|\psi\rangle + \tilde{g}\sum_{n'}\langle n|H_1|n'\rangle\langle n'|\psi\rangle\,, \quad (2.16)$$

where the relation in (2.7) is used and the completeness of the harmonic oscillator basis in (2.8) is exploited. Next, we need to find an expression for the matrix elements of the interaction potential H_1 in the harmonic oscillator basis, corresponding to the overlap integrals according to

$$\begin{aligned}(H_1)_{nn'} \equiv \langle n|\, H_1\, |n'\rangle &= \int \mathrm{d}x \int \mathrm{d}x'\, \langle n|x\rangle\langle x|H_1|x'\rangle\langle x'|n'\rangle = \\ &= \ell\hbar\omega \int \mathrm{d}x \int \mathrm{d}x'\, \psi_n^*(x)\,\delta(x-x')\,\delta(x)\,\psi_{n'}(x') = \ell\hbar\omega\,\psi_n(0)\,\psi_{n'}(0),\end{aligned} \quad (2.17)$$

where the completeness relation of the position basis is exploited twice. The position wavefunctions defined in (2.9) are also used, and since the wavefunction is real, we have $\psi_n^*(0) = \psi_n(0)$. As seen in the expression for $\psi_n(x)$, at the origin ($x = 0$) we have $\psi_n(0) \sim H_n(0)$, where the explicit expressions for the Hermite polynomials at $x = 0$ [19, p. 106] are

$$H_n(0) = \begin{cases} (-1)^m \frac{(2m)!}{m!} & \text{if } n \text{ is even } (n = 2m), \\ 0 & \text{if } n \text{ is odd}, \end{cases} \quad (2.18)$$

hence $\psi_n(0) = 0$ if n is odd. Therefore, the matrix elements of the interaction potential, $(H_1)_{nn'}$, becomes zero if either n or n' (or both) are odd. Hence, we notice that $e = e_n$ in (2.16) if either n or n' are odd, and thus the Schrödinger equation is solved. The exact same situation appears if $\tilde{g} = 0$. Henceforth, the rest of the derivation is only valid if $\tilde{g} \neq 0$ and n, n' are both even. Thus we replace $n \to 2n$ and $n' \to 2n'$ and let $n, n' \in \mathbb{N}$. Combining (2.16) and (2.17) as well as introducing the overlap integral $c_n = \langle n|\psi\rangle$ we obtain

$$(e - e_{2n})c_{2n} = \tilde{g}\ell\psi_{2n}(0)\sum_{n'=0}^{\infty}\psi_{2n'}(0)c_{2n'} \implies c_{2n} = \frac{\tilde{g}\ell\,\psi_{2n}(0)}{e - e_{2n}}\sum_{n'=0}^{\infty}\psi_{2n'}(0)c_{2n'}, \quad (2.19)$$

where we have just reordered the terms. Also notice that n and n' are even and that $\tilde{g} \neq 0$ due to our previous assumptions, thus making $e \neq e_{2n}$. Multiplying the expression in (2.19) with $\psi_{2n}(0)$, then summing over all n, yields

$$\sum_{n=0}^{\infty}\psi_{2n}(0)c_{2n} = \tilde{g}\ell\left(\sum_{n=0}^{\infty}\frac{\psi_{2n}^2(0)}{e - e_{2n}}\right)\left(\sum_{n'=0}^{\infty}\psi_{2n'}(0)c_{2n'}\right), \quad (2.20)$$

where the sum on the left-hand side and the sum to the right cancel each other out. Now using that $e_{2n} = 2n + \frac{1}{2}$, we obtain

$$1 = \frac{\tilde{g}\ell}{2}\sum_{n=0}^{\infty}\frac{\psi_{2n}^2(0)}{\frac{e}{2} - \frac{1}{4} - n} \overset{(2.11)}{=} -\frac{\tilde{g}}{2\sqrt{\pi}}\sum_{n=0}^{\infty}\frac{H_{2n}^2(0)}{2^{2n}\,(2n)!}\left(n + \frac{1}{4} - \frac{e}{2}\right)^{-1}, \quad (2.21)$$

where we have used the normalized wave functions in (2.11). In order to change the dependence of n in (2.21), the following integral representation of $1/z$ is used

$$\frac{1}{z} = \int_0^\infty \frac{\mathrm{d}y}{(1+y)^2} \left(\frac{y}{1+y}\right)^{z-1}, \tag{2.22}$$

which is valid for $z > 0$ [5, eq. 11]. We then apply this to our expression in (2.21) by replacing $z = n + \frac{1}{4} - \frac{e}{2}$, yielding

$$\begin{aligned} -\frac{2}{\tilde{g}} &= \frac{1}{\sqrt{\pi}} \sum_{n=0}^{\infty} \frac{H_{2n}^2(0)}{2^{2n}\,(2n)!} \int_0^\infty \frac{\mathrm{d}y}{(1+y)^2} \left(\frac{y}{1+y}\right)^{n-\frac{e}{2}-\frac{3}{4}} \\ &\overset{(2.18)}{=} \frac{1}{\sqrt{\pi}} \int_0^\infty \frac{\mathrm{d}y}{(1+y)^2} \left(\frac{y}{1+y}\right)^{-\frac{e}{2}-\frac{3}{4}} \sum_{n=0}^{\infty} \frac{(2n)!}{2^{2n}\,(n!)^2} \left(\frac{y}{1+y}\right)^n. \end{aligned} \tag{2.23}$$

The sum can be calculated analytically and by looking at the *Legendre duplication formula* [20, eq. 13.54], we find that

$$\Gamma(z+1)\,\Gamma\Big(z+\frac{1}{2}\Big) = \frac{\sqrt{\pi}}{2^{2z}}\Gamma(2z+1) \implies \frac{\Gamma(2z+1)}{2^{2z}\,\Gamma(z+1)^2} = \frac{\Gamma(z+\frac{1}{2})}{\Gamma(\frac{1}{2})\Gamma(z+1)}, \tag{2.24}$$

where $\Gamma(z)$ is the *Gamma function* and we know that $\Gamma(\frac{1}{2}) = \sqrt{\pi}$. Now using the Gamma function definition of the factorials, i.e. $n! = \Gamma(n+1)$, the expression in (2.24) simplifies to

$$\frac{(2n)!}{2^{2n}\,(n!)^2} = \frac{(n-\frac{1}{2})!}{(-\frac{1}{2})!\,n!}. \tag{2.25}$$

The *associated Laguerre polynomials* [20, eq. 18.64], have the following explicit expression at $x = 0$

$$L_n^{(\alpha)}(0) = \binom{n+\alpha}{n} = \frac{(n+\alpha)!}{\alpha!\,n!}, \tag{2.26}$$

and hence by combining the expressions in (2.25) and (2.26) we obtain

$$\frac{(2n)!}{2^{2n}\,(n!)^2} = L_n^{-1/2}(0). \tag{2.27}$$

Thus, the expression in (2.23) can be written as

$$-\frac{2}{\tilde{g}} = \frac{1}{\sqrt{\pi}} \int_0^\infty \frac{\mathrm{d}y}{(1+y)^2} \left(\frac{y}{1+y}\right)^{-\frac{e}{2}-\frac{3}{4}} \sum_{n=0}^{\infty} L_n^{-1/2}(0) \left(\frac{y}{1+y}\right)^n. \tag{2.28}$$

Now we can exploit the generating function for the *associated Laguerre polynomials* [21, p. 268], namely

$$\sum_{n=0}^{\infty} L_n^{(\alpha)}(x)\,t^n = \frac{\mathrm{e}^{-xt/(1-t)}}{(1-t)^{\alpha+1}}, \tag{2.29}$$

by using $x = 0$, $\alpha = -1/2$ and $t = \frac{y}{1+y}$ such that the expression in (2.28) simplifies to

$$-\frac{2}{\tilde{g}} = \frac{1}{\sqrt{\pi}} \int_0^\infty \frac{\mathrm{d}y}{(1+y)^2} \left(\frac{y}{1+y}\right)^{-\frac{e}{2}-\frac{3}{4}} \left(1 - \frac{y}{1+y}\right)^{-1/2} = \frac{1}{\sqrt{\pi}} \int_0^\infty \frac{\mathrm{d}y\, y^{-\frac{3}{4}-\frac{e}{2}}}{(1+y)^{\frac{3}{4}-\frac{e}{2}}}. \quad (2.30)$$

The integral above may be expressed using the *confluent hypergeometric function* $U(a, b, z)$ at $z = 0$ [20, eq. 18.137, 18.142, 18.145], according to

$$\begin{aligned} \Gamma(a)\, U(a, b, 0) &= \int_0^\infty t^{a-1} (1+t)^{b-a-1}\, \mathrm{d}t, \\ U(a, b, 0) &= \frac{\pi}{\sin(\pi b)} \frac{1}{\Gamma(1+a-b)\Gamma(b)}. \end{aligned} \quad (2.31)$$

Using $a = \frac{1}{4} - \frac{e}{2}$, $b = \frac{1}{2}$, we solve the integral and obtain the following relation

$$-\frac{2}{\tilde{g}} = \frac{1}{\sqrt{\pi}} \frac{\pi}{\sin\left(\frac{\pi}{2}\right)} \frac{\Gamma\left(\frac{1}{4} - \frac{e}{2}\right)}{\Gamma\left(\frac{3}{4} - \frac{e}{2}\right)\Gamma\left(\frac{1}{2}\right)} = \frac{\Gamma\left(\frac{1}{4} - \frac{e}{2}\right)}{\Gamma\left(\frac{3}{4} - \frac{e}{2}\right)}, \quad (2.32)$$

where we once again use that $\Gamma(\frac{1}{2}) = \sqrt{\pi}$. Finally, the dimensionless energy e of the system is given by the following transcendental equation

$$-\frac{2}{\tilde{g}} = \frac{\Gamma\left(\frac{1}{4} - \frac{e}{2}\right)}{\Gamma\left(\frac{3}{4} - \frac{e}{2}\right)}. \quad (2.33)$$

The analytical energy spectrum is presented in Fig. 2.1, as a function of the interaction strength g. We have a quantized energy spectrum for every value of the interaction strength. The solid lines correspond to the energies for states with even parity E_i^+ obtained from the transcendental equation in (2.33). In addition, the dotted lines correspond to energies for odd parity states E_i^-, with the energies equaling the Harmonic oscillator energies (2.7), i.e. $E_i^- = E_n$ for $n = 2i + 1$. The energy level is denoted i and is separated for the even and odd parity states, meaning that we denote E_i^+ and E_i^- as separate energy spectra. Notice that the energy of the odd parity states is trivial since it does not depend on the interaction strength. Henceforth, in this study we are only interested in the even parity states and the even parity energy will simply be denoted as $E_i^+ \equiv E_i$. A more physical intuition to why the odd parity states does not depend on g is by realizing that the wave function in relative coordinates, $\psi(x) \equiv \langle x|\psi\rangle$ of an odd parity state has to be an odd function, implying that $\psi(0) = 0$. Since the interaction is modeled with $g\delta(x)$ and hence only contributing at $x = 0$ the odd parity energy cannot depend on g.

Also, worth mentioning is that two nearby energy levels connect at $g = \infty$ and $g = -\infty$. This means that the energy of the ground state at infinite repulsive interaction is the same as the energy of the first excited state at infinite attractive interaction, i.e. $E_0(\infty) = E_1(-\infty)$. The ground state energy also diverges as $g \longrightarrow -\infty$, since the atoms becomes infinitely attracted to each other and hence the system becomes infinitely bound.

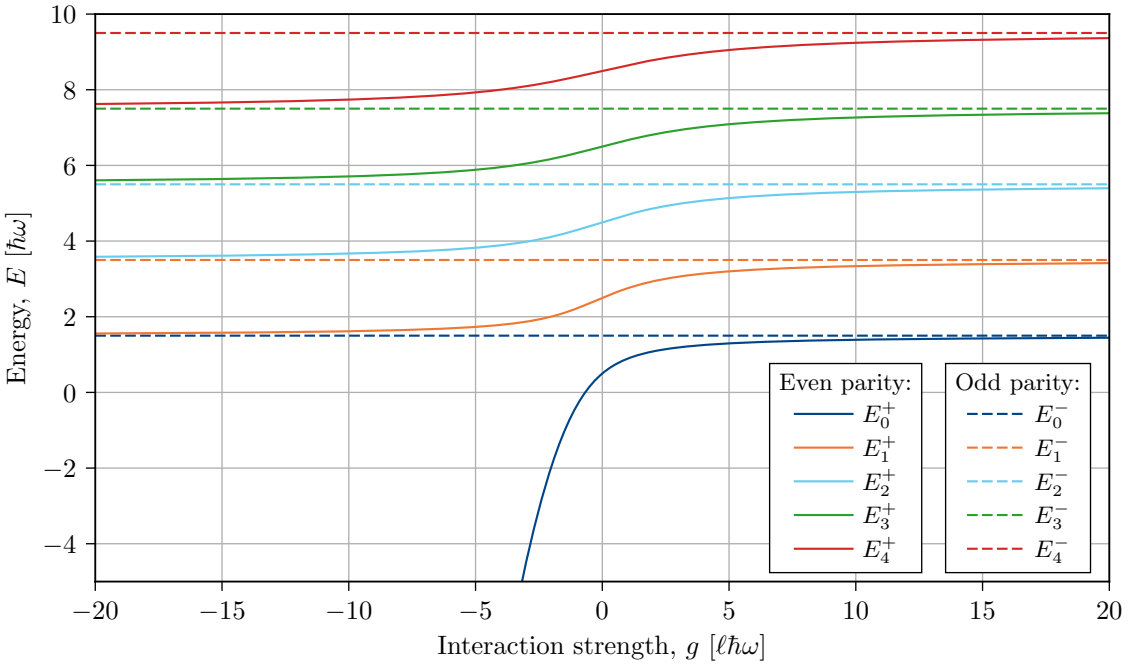

Figure 2.1: The low-lying part of the analytical energy spectrum as a function of the interaction strength g, where the solid (dotted) lines correspond to the energies for states with even (odd) parity E_i^+ (E_i^-). The even parity energies are obtained from solving the transcendental equation in (2.33). Further, note that the odd parity energies do not depend on the interaction strength, but instead equals the harmonic oscillator energies (2.7) with $E_i^- = E_n$ for $n = 2i + 1$.

2.1.3 Numerical solution

In order to construct the eigenvector continuation emulator, and to be able to measure its performance, we first need to determine the eigenstates and energy eigenvalues of the Hamiltonian (2.4) numerically as a function of the interaction strength g using exact diagonalization. Therefore, we want to find an expression for the matrix elements of the Hamiltonian, making the Schrödinger equation an eigenvalue problem. Seeing that $|n\rangle$ are eigenstates of H_0 in (2.4), we choose to express our Hamiltonian matrix using the harmonic oscillator basis. Therefore, we make a spectral decomposition of our quantum state

$$|\psi\rangle = \sum_{n=0}^{\infty} |n\rangle \underbrace{\langle n|\psi\rangle}_{\equiv c_n} = \sum_{n=0}^{\infty} c_n |n\rangle \approx \sum_{n=0}^{2N-1} c_n |n\rangle \,, \tag{2.34}$$

where c_n denotes the decomposition coefficient (overlap integral), the same as in the derivation of the analytical energy. In the above expression, we have also made an approximation by making a finite truncation of the sum. Using this decomposition, the Schrödinger equation in (2.15) may be rewritten as

$$\sum_{n=0}^{2N-1} (H_0 + \tilde{g}H_1) c_n |n\rangle = e\hbar\omega \sum_{n=0}^{2N-1} c_n |n\rangle \,. \tag{2.35}$$

Now multiplying with $\langle n'|$ from the left and renaming $n \leftrightarrow n'$ yields

$$\sum_{n'=0}^{2N-1} \underbrace{\langle n|H_0 + \tilde{g}H_1|n'\rangle}_{\equiv \mathcal{H}_{nn'}} c_{n'} = e \sum_{n'=0}^{2N-1} c_{n'} \underbrace{\langle n|n'\rangle}_{=\delta_{nn'}} \implies \sum_{n'=0}^{2N-1} \mathcal{H}_{nn'}\, c_{n'} = e\, c_n. \tag{2.36}$$

We notice that this corresponds to an eigenvalue problem, with the decomposition coefficients as the eigenvectors, i.e.

$$\mathcal{H}\,\vec{c} = e\,\vec{c}, \qquad \text{where } \vec{c} = [c_0, c_1, c_2, \cdots c_{2N-1}]^T. \tag{2.37}$$

The matrix elements of $\mathcal{H}$ in the harmonic oscillator basis correspond to the overlap integrals

$$\mathcal{H}_{nn'} \equiv \langle n|\mathcal{H}|n'\rangle = \langle n|H_0|n'\rangle + \tilde{g}\,\langle n|H_1|n'\rangle \equiv (H_0)_{nn'} + \tilde{g}\,(H_1)_{nn'}. \tag{2.38}$$

The matrix element of H_0 in the harmonic oscillator basis is trivial, since $|n\rangle$ are eigenstates of H_0. According to (2.7) and (2.8) it becomes

$$(H_0)_{nn'} \equiv \langle n|H_0|n'\rangle = \delta_{nn'}\, E_n = \delta_{nn'} \left(n + \frac{1}{2}\right)\hbar\omega. \tag{2.39}$$

Using the expression in (2.17) the matrix elements of the interaction Hamiltonian H_1 are

$$(H_1)_{nn'} \equiv \langle n|H_1|n'\rangle = \ell\hbar\omega\psi_n(0)\psi_{n'}(0) = \frac{\hbar\omega}{\sqrt{\pi}} \frac{H_n(0)\, H_{n'}(0)}{\sqrt{2^{n+n'} n! n'!}}. \tag{2.40}$$

As we see in (2.18), $H_n(0) = 0$ if n is odd, which implies that $(H_1)_{nn'} = 0$ if either n or n' are odd. Hence, we want to find the expression for even values of n and n'. We therefore use the expression in (2.18), replacing $n \leftrightarrow 2n$ and $n' \leftrightarrow 2n'$, which results in

$$\langle 2n|H_1|2n'\rangle = (-1)^{n+n'} \frac{\hbar\omega}{\sqrt{\pi}} \left[\frac{(2n)!\,(2n')!}{2^{2n+2n'}\,(n!)^2\,(n'!)^2}\right]^{1/2}. \tag{2.41}$$

Using the relation in (2.25), obtained from the Legendre duplication formula, the matrix element can be expressed as a fraction of Gamma functions according to

$$\langle 2n|H_1|2n'\rangle = (-1)^{n+n'} \frac{\hbar\omega}{\pi} \left[\frac{\Gamma\left(n+\frac{1}{2}\right)\,\Gamma\left(n'+\frac{1}{2}\right)}{\Gamma(n+1)\,\Gamma(n'+1)}\right]^{1/2}. \tag{2.42}$$

Notice that this is separable, i.e. $\langle 2n|H_1|2n'\rangle = f(n)\,f(n')$, which enables the matrix to be written as an outer product. This makes the computation of the Hamiltonian matrix efficient by utilizing the `NumPy` [13] method `outer`[3] in the `Python` implementation. In addition, the Gamma functions in the above expression becomes extremely large for large values of m. Therefore, in the numerical calculations, we use the logarithm of the Gamma functions by exploiting the `SciPy` [14] method `gammaln`[4].

[3] The documentation of the method is found at:
`https://numpy.org/doc/stable/reference/generated/numpy.outer.html`

[4] The documentation of the method is found at:
`https://docs.scipy.org/doc/scipy/reference/generated/scipy.special.gammaln.html`

As we concluded, for odd n, the matrix elements only yield a non-zero contribution if $n = n'$. The Hamiltonian matrix may be rearranged into two block-diagonal parts, with each part corresponding to matrix elements obtained from even and odd n, respectively. This is equivalent of the previous discussion of the even and odd parity states in the derivation of the analytical expression and the even (odd) parity states are obtained from the block diagonal part corresponding to even (odd) number states. The odd parity part hence become diagonal, yielding the harmonic oscillator energies E_n as eigenvalues. Therefore, we are only interested in the part yielding even parity states, reducing the dimensionality of the eigenvalue problem from $2N \times 2N$ to $N \times N$, where N henceforth denotes the dimension of the Hamiltonian matrix. Now we only need to sum over the decomposition coefficients corresponding to even n to obtain the even parity state

$$|\psi\rangle = \sum_{n=0}^{N-1} c_{2n} \, |2n\rangle \, . \tag{2.43}$$

The desired eigenenergies and eigenvectors are obtained by solving the following N-dimensional eigenvalue problem

$$\mathcal{H}\,\vec{c} = e\,\vec{c}, \qquad \text{where } \vec{c} = [c_0, c_2, c_4, \ldots, c_{2N-2}]^T, \tag{2.44}$$

and will be referred to as the *numerical Schrödinger equation*. The eigenvectors $\vec{c}$ can be used to obtain an numerical approximation of the wave function in relative coordinates

$$\psi(x) \equiv \langle x \,|\, \psi \rangle = \sum_{n=0}^{N-1} c_{2n} \, \langle x \,|\, 2n \rangle \overset{(2.9)}{=} \sum_{n=0}^{N-1} c_{2n} \psi_n(x). \tag{2.45}$$

We defined the relative energy error ε between the analytical energy obtained by solving the transcendental equation in (2.33) and the numerical energy by solving the eigenvalue problem in (2.44) using exact diagonalization as

$$\varepsilon = \frac{E_{\text{numerical}} - E_{\text{analytical}}}{|E_{\text{analytical}}|}, \tag{2.46}$$

where the numerator is always greater or equal to zero due to the *variational principle*. The denominator contains the absolute value of $E_{\text{analytical}}$ to ensure that ε always remains positive, even for negative energies. In Fig. 2.2, the relative ground state energy error, ε is plotted against the size of the matrix N for different values of the interaction strength. We notice that the overall convergence is slow, and that the energy error increases as the magnitude of g increases. The error is especially large for strongly attractive systems.

Since the main intention of this study is to explore the method of eigenvector continuation—which will be showed in Ch. 3 cannot outperform the energy obtained from exact diagonalization—the precision compared to the analytical energy does not play a crucial role here. Therefore, we conclude that using $N = 5 \times 10^4$ yields enough precision for this study without being extremely computational heavy. Henceforth, E and c_n will denote the energy and eigenvector obtained from solving

the numerical Schrödinger equation (2.44), respectively, while $|\psi\rangle$ will denote the numerical eigenstate (2.43).

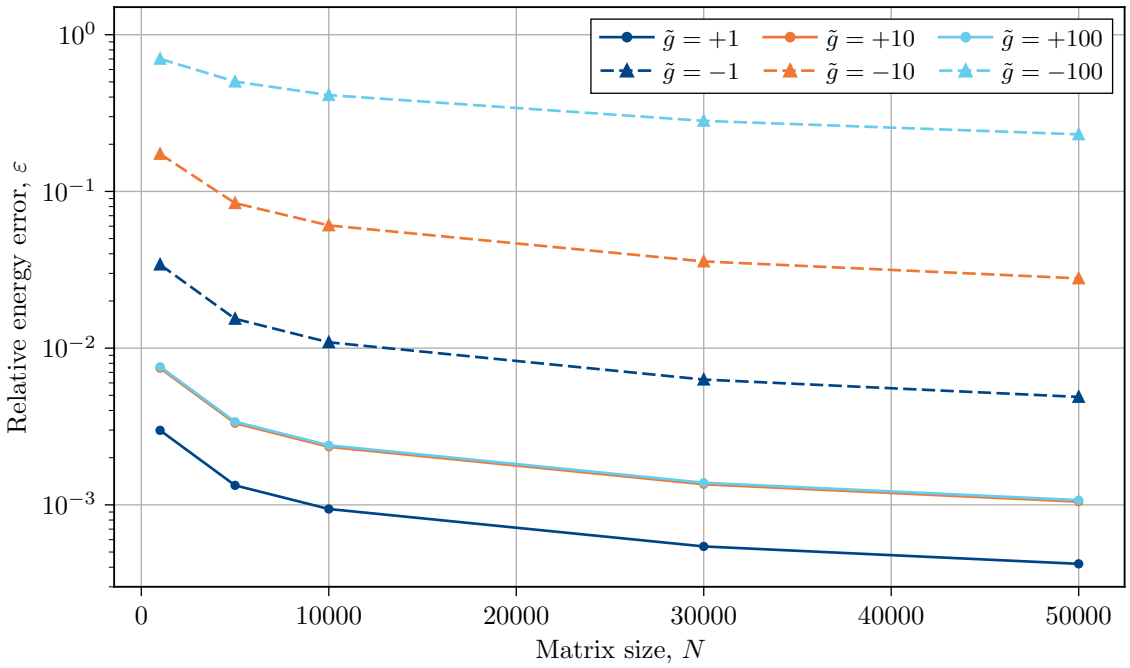

Figure 2.2: The relative ground state energy error between the analytical energy and the numerical energy, ε plotted against the size of the matrix N for different values of the interaction strength.

2.2 Generalized many-body system

In addition to the ultracold system of two atoms, we will also consider a many-body generalization of the Busch model. The many-body theory and detailed derivation of the many-body Hamiltonian matrix elements are beyond the scope of this project. Instead, we use an already implemented code to obtain the Hamiltonian matrices, written in `C++` by *J. Lindgren* [15]. However, this code have been made accessible as a `Python` module with `pybind11` [22]. Here, we will only present a summary of how to obtain the many-body Hamiltonian matrices, while a much more in-depth description is given in [6], [15].

The many-body system is realized in a similar way as the two-body system described earlier, with ultracold atoms in a harmonic oscillator trap with a tunable zero-range interaction. However, now we consider a mixture of fermionic atoms of two different species, where fermions of the same species are indistinguishable, i.e. identical, wihle fermions of different species are distinguishable. We restrict ourselves to the case where the pairwise interatom interaction only occurs between atoms of different species. This means that the identical atoms do not interact with each other. Thus,

the Hamiltonian of this generalized many-body system becomes

$$\mathcal{H} = \underbrace{\sum_{k=0}^{n_\uparrow}\left(\frac{p_{\uparrow,k}^2}{2m}+\frac{m\omega^2}{2}x_{\uparrow,k}^2\right)+\sum_{k=1}^{n_\downarrow}\left(\frac{p_{\downarrow,k}^2}{2m}+\frac{m\omega^2}{2}x_{\downarrow,k}^2\right)}_{\equiv H_0} + \underbrace{\tilde{g}\sum_{k_\uparrow=1}^{n_\uparrow}\sum_{k_\downarrow=1}^{n_\downarrow}V_{k_\uparrow,k_\downarrow}}_{\equiv H_1}, \tag{2.47}$$

where $\uparrow\downarrow$ denotes the two species, and the interaction $V_{k_\uparrow,k_\downarrow} = \delta(x_{\uparrow,k_\uparrow} - x_{\downarrow,k_\downarrow})$ only yields a non-zero contribution if atoms of different species are located at the same position. Moreover, the number of particles is denoted $n_\uparrow$ and $n_\downarrow$, respectively, and a similar notation denotes the momentum and position operators. Just as in (2.14), the Hamiltonian depends linearly on the dimensionless interaction strength $\tilde{g}$

$$\mathcal{H} = H_0 + \tilde{g}H_1 \equiv \mathcal{H}(\tilde{g}). \tag{2.48}$$

The many-body basis states $|\phi_\alpha\rangle$ for n indistinguishable fermionic atoms of one species is now constructed using *single particle states*

$$|\phi_\alpha\rangle = \mathcal{A}\,|m_1\rangle \otimes |m_2\rangle \otimes \cdots \otimes |m_n\rangle \equiv |(m_1, m_2, \ldots, m_n)\rangle_{\mathcal{A}}\,, \tag{2.49}$$

where $\alpha = \uparrow\downarrow$ and the states $|m_k\rangle$ are eigenstates of H_0. Since the atoms are indistinguishable fermions, the product state in (2.49) is antisymmetrized with the antisymmetrizer $\mathcal{A}$. The basis state of the full system, i.e. including both species will thus be the tensor product of the basis states in (2.49) yielding

$$|\phi_\uparrow\rangle \otimes |\phi_\downarrow\rangle = |(m_1, m_2, \ldots, m_{n_\uparrow})\rangle_{\mathcal{A}} \otimes |(k_1, k_2, \ldots, k_{n_\downarrow})\rangle_{\mathcal{A}}\,. \tag{2.50}$$

Since the many-body basis states are eigenstates of H_0, the Hamiltonian matrix elements of H_0 once again become trivial. However, since the pairwise interaction between the distinguishable atoms is modeled using a delta function, we need to convert from the single-particle states to some relative coordinates, similar to what we did in (2.2) and (2.3) in order to find the matrix elements of the interaction Hamiltonian H_1. That is, we need to find the many-body equivalent of (2.40). For every pair of interacting atoms, the kinetic energy and potential energy due to the harmonic oscillator trap is described by the Hamiltonian

$$H = \frac{p_1^2}{2m_1} + \frac{p_2^2}{2m_2} + m_1\omega\,\frac{x_1^2}{2} + m_2\omega\,\frac{x_2^2}{2}, \tag{2.51}$$

where 1 and 2 denotes the two atoms in the pairwise interaction, respectively. Where the number operator for atom 1 and 2 become

$$\begin{aligned}
&\text{Atom 1:}\quad n_1 = a_1 a_1^\dagger, \quad a_1 = \frac{m\omega}{2\hbar}\left(x_1 + \frac{\mathrm{i}p_1}{m\omega}\right), \quad a_1^\dagger = \frac{m\omega}{2\hbar}\left(x_1 - \frac{\mathrm{i}p_1}{m\omega}\right),\\
&\text{Atom 2:}\quad n_2 = a_2 a_2^\dagger, \quad a_2 = \frac{m\omega}{2\hbar}\left(x_2 + \frac{\mathrm{i}p_2}{m\omega}\right), \quad a_2^\dagger = \frac{m\omega}{2\hbar}\left(x_2 - \frac{\mathrm{i}p_2}{m\omega}\right).
\end{aligned} \tag{2.52}$$

Just as in (2.2), the Hamiltonian H can be transformed into

$$H = \frac{p^2}{2\mu} + \mu\omega\frac{x^2}{2} + \frac{P^2}{2M} + M\omega\frac{X^2}{2}, \tag{2.53}$$

using the so-called *Jacobi coordinates* in (2.2). In these coordinates, we define the relative (Rel.) and center of mass (CM) number operators

$$\begin{aligned} &\text{Rel:} \quad n = aa^\dagger, \qquad a = \frac{m\omega}{2\hbar}\left(x + \frac{\mathrm{i}p}{m\omega}\right), \qquad a^\dagger = \frac{m\omega}{2\hbar}\left(x - \frac{\mathrm{i}p}{m\omega}\right), \\ &\text{CM:} \quad N = AA^\dagger, \qquad A = \frac{m\omega}{2\hbar}\left(X + \frac{\mathrm{i}P}{m\omega}\right), \qquad A^\dagger = \frac{m\omega}{2\hbar}\left(X - \frac{\mathrm{i}P}{m\omega}\right). \end{aligned} \tag{2.54}$$

Both the single particle and Jacobi coordinates can thus be expressed in terms of harmonic oscillator states $|n_1\rangle\otimes|n_2\rangle \equiv |n_1, n_2\rangle$ and $|N\rangle\otimes|n\rangle \equiv |N, n\rangle$, respectively[5]. The transformation between these coordinates is obtained through utilizing the completeness of $|n_1, n_2\rangle$, namely

$$|N, n\rangle = \sum_{n_1,n_2} |n_1, n_2\rangle \langle n_1, n_2 \,|\, N, n\rangle . \tag{2.55}$$

Exploiting this expression, together with the the defined number operators in (2.52) and (2.54) one can calculate the overlap integrals between the Jacobi and single particle coordinates, yielding

$$\langle N, n \,|\, n_1, n_2\rangle = \underbrace{\sqrt{\frac{n_1!n_2!}{N!n!}} 2^{-(N+n)/2} \sum_{k=a}^{b} (-1)^{n_1-k} \binom{N}{k} \binom{n}{n_1-k}}_{\equiv m(N,n_1,n_2)} \delta_{N+n,n_1+n_2}, \tag{2.56}$$

where $a = \max\{0, n_1 - n\}$ and $b = \min\{N, n_1\}$ [6, eq. 2.52]. Using the completeness of $|N, n\rangle$ we obtain

$$\langle n_1, n_2 \,|\, H_1 \,|\, n_1', n_2'\rangle = \sum_{N=0}^{c} \langle n_1 + n_2 - N \,|\, H_1 \,|\, n_1' + n_2' - N\rangle \, m(N, n_1, n_2) \, m(N, n_1', n_2') \tag{2.57}$$

where $c = \min\{n_1 + n_2, n_1' + n_2'\}$ [6, eq. 2.54]. This is the expression for the matrix elements of the interaction Hamiltonian H_1 in the single particle coordinates, where $\langle n_1 + n_2 - N \,|\, H_1 \,|\, n_1' + n_2' - N\rangle$ is calculated according to (2.40). Due to the *Kronecker delta* in (2.56), the matrix elements of H_1 simply become a sum over N.

In (2.43) the number of even parity harmonic oscillator basis states N directly translates to the Hamiltonian matrix size. However, now in the case of the many-body basis state, the truncation is given by $N_{\max}$, which is the total energy quanta cutoff in harmonic oscillator units ($\hbar\omega$). This means that the total energy quanta of the many-body basis states in (2.50) is less than or equal to $N_{\max}$. Due to the larger number of particles, the combinatorial size of the problem increases rapidly as $N_{\max}$ increased. Therefore, we end up with a larger dimensional eigenvalue problem and hence more costly to solve computationally. Thus, as a limitation, the number of atoms of one species will be constant to one. Without loss of generality, we fix $n_\downarrow = 1$. The studied systems will henceforth be denoted as $n_\uparrow + 1$, meaning that we consider a system with n_1 indistinguishable fermions that pairwise interact with one impurity fermion. This means that the two-body system considered in Sec. 2.1 corresponds to the generalized many-body system denoted $1 + 1$.

[5] Do not confuse this with the matrix size N defined in Sec. 2.1, and used throughout this thesis.

3. Eigenvector continuation

In this chapter the method of *eigenvector continuation* (EVC) [1] is presented together with an explanation of how it can be used to construct an emulator for solving the energy of the ultracold atomic system described in Ch. 2. However, a detailed and rigorous mathematical motivation and description of EVC is not within the scope of this project[1]. Therefore, this chapter will focus on the theory and motivation behind EVC.

3.1 Purpose of using an emulator

As presented in (2.14) and (2.48), the Hamiltonian of both the two and many-particle system depends linearly on the real parameter $\tilde{g}$, the dimensionless interaction strength, according to

$$\mathcal{H}(\tilde{g}) = H_0 + \tilde{g}\, H_1. \tag{3.1}$$

We aim to investigate how the energy spectrum depends on the tunable interaction strength $\tilde{g}$, focusing in particular on the ground state energy $E_0(\tilde{g})$[2]. Thus, for every value of $\tilde{g}$, a new Hamiltonian is obtained which yields a new eigenvalue problem according to the Schrödinger equation

$$\mathcal{H}(\tilde{g})\,|\psi_i(\tilde{g})\rangle = E_i(\tilde{g})\,|\psi_i(\tilde{g})\rangle\,, \tag{3.2}$$

where the dependence on the interaction parameter is made explicit. EVC has been proposed as a very efficient and accurate emulator for solving the energy eigenvalues, and other observables, of quantum systems as some linear parameter is varied [2]. Thus, potentially yielding a significant speedup in the calculations of the energy eigenvalues $E_i(\tilde{g})$ in (3.2).

In Sec. 2.1.2, we showed that there is an analytical solution to the two-body system, and we also showed that we can calculate an approximate numerical solution. For the many-body system there is no general exact solution, but we can again use numerical diagonalization to obtain an approximate solution. The aim of this study to investigate if, and how well, EVC can be used as an emulator to predict $E(g)$ for the two- and many-body system. This analysis requires the result from exact diagonalization to compare with the EVC predictions.

3.2 Theory and implementation

The method of EVC is initiated by solving the N-dimensional eigenvalue problem using *exact diagonalization* (ED) for $m \ll N$ values of the interaction strength, i.e.

[1] For interested readers, you can find more information in [1], [23], [24]

[2] The ground state energy is denoted E_0, the first excited state E_1 and so forth.

$\tilde{g}_{\text{tp}} \in \{\tilde{g}_1, \tilde{g}_2, \ldots, \tilde{g}_m\}$. These values are denoted *training points* (tp), and using the eigenstates at these points we obtain a d-dimensional subspace S of the total Hilbert space

$$S = \text{span}\left\{|\psi_1\rangle, |\psi_2\rangle, \ldots, |\psi_d\rangle\right\}, \tag{3.3}$$

where $|\psi_k\rangle = |\psi_i(\tilde{g}_j)\rangle$. Note that every k corresponds to a unique duplet of i and j, $k = (i, j)$. The subspace can consist of states from different interaction strengths $\tilde{g}_j$, but also from different excitations. Thus, $m \leq d$, where equality is obtained only when a single state (in practice the ground state) is used for every value of $\tilde{g}_j$. The eigenstates $|\psi_k\rangle$ spanning S will be denoted *training vectors*, and are used to construct the $N \times d$-matrix

$$X \equiv \begin{bmatrix} | & | & & | \\ |\psi_1\rangle & |\psi_2\rangle & \ldots & |\psi_d\rangle \\ | & | & & | \end{bmatrix}. \tag{3.4}$$

It is important to notice that these states are in general not orthogonal, i.e. $\langle\psi_k|\psi_{k'}\rangle \neq \delta_{kk'}$. The concept of EVC is to approximate the full solution $|\psi(\tilde{g})\rangle$ with a subspace projected state, denoted $|\tilde{\phi}(\tilde{g})\rangle$. Thus, we approximate a general eigenstate to be a linear combination of the training vectors

$$|\psi(\tilde{g})\rangle \approx |\tilde{\phi}(\tilde{g})\rangle = \sum_{i=1}^{d} \beta_i(\tilde{g})\,|\psi_i\rangle = X\beta(\tilde{g}), \tag{3.5}$$

where $\beta(\tilde{g})$ is a coefficient vector and $|\tilde{\phi}\rangle = X\beta$ is the so-called *Ritz vector* [25]. This can be a good approximation if $|\psi\rangle$ has a large overlap with the subspace S, and will be a rather poor approximation otherwise. Fortunately, eigenvectors will follow a smooth trajectory in the full Hilbert space as continuous parameters in the Hamiltonian are varies. This implies that significant overlaps with the training vectors are guaranteed in most situations (see [1], [24] for details). Note, however, that the subspace projected state (3.5) is not in general an eigenstate[3] of the Hamiltonian in (3.2). Thus, by replacing the energy E with the so-called *Ritz value* $\tilde{E}$, we obtain

$$\mathcal{H}(\tilde{g})\,|\tilde{\phi}_i(\tilde{g})\rangle = \tilde{E}_i(\tilde{g})\,|\tilde{\phi}_i(\tilde{g})\rangle\,. \tag{3.6}$$

The equation in (3.6) is an under-determined system, since $d \ll N$ and to find the best solution we apply the so-called *Ritz method* [25], [26]. This approach can be derived from either a quantum mechanical or a mathematical point of view using the *variaional method* or the *Galerkin method*, respectively.

Variational method

We use the Ritz vector $|\tilde{\phi}(\tilde{g})\rangle$ in (3.5) as a *trial wave function* and exploit the *variation principle*, i.e.

$$E(\tilde{g}) \leq \tilde{E}(\tilde{g}) = \frac{\langle\tilde{\phi}(\tilde{g})\,|\,\mathcal{H}(\tilde{g})\,|\,\tilde{\phi}(\tilde{g})\rangle}{\langle\tilde{\phi}(\tilde{g})\,|\,\tilde{\phi}(\tilde{g})\rangle}, \tag{3.7}$$

[3] It is indeed only an eigenstate if and only if the $|\psi\rangle$ lives within the subspace S.

where β_i in the expression for $|\tilde{\phi}(\tilde{g})\rangle$ in (3.5) are viewed as *variational coefficients* [26]. We want to find the minimum of $\tilde{E}(\tilde{g})$ with respect to the variational coefficients. The minimum of the right-hand side of (3.7) with respect to β_i is given by the solution to the *generalized eigenvalue problem*

$$\tilde{\mathcal{H}}(\tilde{g})\beta(\tilde{g}) = \tilde{E}(\tilde{g})\mathcal{N}\beta(\tilde{g}), \tag{3.8}$$

of dimension $d \times d$. On the left-hand side we have the d-dimensional subspace projected Hamiltonian

$$\tilde{\mathcal{H}}(\tilde{g}) \equiv X^\dagger \mathcal{H}(\tilde{g}) X, \tag{3.9}$$

with the matrix elements $\tilde{\mathcal{H}}_{ij} = \langle\psi_i|\mathcal{H}(\tilde{g})|\psi_j\rangle$. Furthermore, on the right-hand side we have the norm matrix

$$\mathcal{N} \equiv X^\dagger X, \tag{3.10}$$

where $\mathcal{N}_{ij} = \langle\psi_i|\psi_j\rangle$. The Ritz value and vector are hence obtained by solving the generalized eigenvalue problem and are used as approximations of the energy and wave function, respectively. Namely $E_i(\tilde{g}) \approx \tilde{E}_i(\tilde{g})$ and $|\tilde{\phi}(\tilde{g})\rangle \approx X\beta(\tilde{g})$, and due to the *variational principle* in (3.7), we are guaranteed that $E(\tilde{g}) \leq \tilde{E}(\tilde{g})$ [26].

Galerkin method

Another derivation in finding the best solution to the problem in (3.6) is by exploiting the *Galerkin conditions*. It states that the residual $r = \mathcal{H}\,|\tilde{\phi}\rangle - \tilde{E}\,|\tilde{\phi}\rangle$ should be orthogonal to the subspace S, i.e.

$$\mathcal{H}(\tilde{g})\,|\tilde{\phi}(\tilde{g})\rangle - \tilde{E}(\tilde{g})\,|\tilde{\phi}(\tilde{g})\rangle \perp S. \tag{3.11}$$

The above expression can equivalently be formulated as the overlap integrals between the residual and the eigenstates spanning S equaling zero, i.e.

$$\langle\psi_i|\left(\mathcal{H}\,|\tilde{\phi}\rangle - \tilde{E}\,|\tilde{\phi}\rangle\right) = 0, \qquad i = 1, \ldots, d. \tag{3.12}$$

Using the definition of the matrix X in (3.4) and exploiting the definition of the Ritz vector $|\tilde{\phi}(\tilde{g})\rangle = X\beta(\tilde{g})$, the expression in (3.12) can be expressed as a matrix representation according to

$$X^\dagger \mathcal{H}(\tilde{g}) X\beta(\tilde{g}) - \tilde{E}(\tilde{g}) X^\dagger X\beta(\tilde{g}) = 0. \tag{3.13}$$

Using the definition of the subspace projected Hamiltonian (3.9) and the norm matrix $\mathcal{N}$ (3.10) we now arrive at the same *generalized eigenvalue problem* as before

$$\tilde{\mathcal{H}}(\tilde{g})\beta(\tilde{g}) = \tilde{E}(\tilde{g})\mathcal{N}\beta(\tilde{g}). \tag{3.8}$$

For other physical systems it has been shown that $\tilde{E}$ is a great approximation of E using only a few training vectors [2]. The predicted energy eigenvalues are obtained by solving the generalized eigenvalue problem [4], and in conclusion we have reduced the large $N \times N$ eigenvalue problem in (3.2) to the much smaller $d \times d$ generalized

eigenvalue problem in (3.8). We will later show that $\tilde{E}(\tilde{g})$ is in general an excellent approximation of $E(\tilde{g})$ for our physical, thus making EVC an efficient *emulator* of the full solution. It is also important to keep in mind that the basis of $|\psi\rangle$ is irrelevant for EVC and will only affect the basis of the obtained Ritz vector $|\tilde{\phi}\rangle$. This is important for our application since in the two-body system we use a relative coordinate basis while in the generalized many-body system the basis is constructed from single-particle states.

3.2.1 Efficiency of an EVC emulator

Since the Hamiltonian $\mathcal{H}(\tilde{g})$ depends linearly on $\tilde{g}$, we can to separate the projection of H_0 and H_1 in (3.9). This makes the EVC emulator much more efficient since we only need to carry out the matrix operations once. Hence, the subspace Hamiltonian can be separated according to

$$\tilde{\mathcal{H}}(\tilde{g}) \equiv X^\dagger \mathcal{H}(\tilde{g}) X = X^\dagger H_0 X + \tilde{g}\, X^\dagger H_1 X \equiv \tilde{H}_0 + \tilde{g}\tilde{H}_1, \tag{3.14}$$

where we only need calculate $\tilde{H}_0$ and $\tilde{H}_1$ once to obtain $\tilde{\mathcal{H}}(\tilde{g})$ for any $\tilde{g}$. Note that $\tilde{H}_0$ and $\tilde{H}_1$ are only $d \times d$-matrices and thus easy to store. However, it is important to note that EVC only requires that a continuous parameter in the model can be varied in order to make predictions by solving the generalized eigenvalue problem (3.8). Hence, the parameter does not necessarily have to be linear but rather the eigenvector trajectory needs to be continuous. Nonetheless, if the parameter is linear, the relation in (3.14) can be exploited and the emulator becomes much more efficient.

3.2.2 Mathematical motivation of eigenvector continuation

By continuously varying the linear parameter $\tilde{g}$ we obtain an eigenvector trajectory $|\psi(\tilde{g})\rangle$ in the N-dimensional Hilbert space. The eigenvector can be viewed as a point in the N-dimensional space, and when $\tilde{g}$ is varied the point moves along a continuous trajectory. The high accuracy of EVC is obtain by exploiting the fact that the trajectory can be efficiently represented in a very low dimensional space compared to the total Hilbert space [1], [4]. This is the cause of the dimensionality reduction between the two eigenvalue problems in (3.2) and (3.8).

In conclusion, EVC provides an efficient approach to interpolate and extrapolate the eigenvector trajectory using only a few training vectors. In general, the precision of the approximation will depend on the overlap between the desired eigenstate and the training vectors.

3.2.3 Limitations when constructing an EVC emulator

One of the main limitations[4] with EVC is that the training vectors spanning S are not necessarily linearly independent and that the actual dimension of the subspace is not guaranteed to equal d, but rather $\dim(S) \leq d$. If the training vectors are

[4] In fact, poles in the so-called S-matrix is a strict limitation—but not discussed here, more information can be found in [1], [24].

linearly dependent, the norm matrix $\mathcal{N}$ will not have full rank. This implies that the matrix will be singular, yielding a non-solvable system in (3.8).

Also, if the training vectors are *almost* linearly dependent the norm matrix $\mathcal{N}$ becomes *ill-conditioned*. This makes the numerical solution to the generalized eigenvalue problem in (3.8) computationally unstable, since at least one eigenvalue of $\mathcal{N}$ will be close to zero. An ill-conditioned matrix is categorized with a too high *condition number*, which will impact the stability and accuracy of the EVC emulator and can make the predictions noisy [24]. A too high condition number will even make the generalized eigenvalue problem in (3.8) numerically unsolvable. Fortunately, this problem is easy to diagnose, and the simplest solution is to just choose different training vectors and construct a new emulator.

3.2.4 Generalization with more parameters

EVC can also be generalized with more parameters. An efficient emulator is obtained once again if the Hamiltonian depends linearly on those parameters, according to

$$\mathcal{H}(\vec{a}) = H_0 + \sum_{i=1}^{p} a_i \, H_i, \tag{3.15}$$

for a system with p parameters. However, the study of such systems is not within the scope of this work.

4. Two-body energy emulations

In this chapter, we present the performance and accuracy of the low-lying energy spectrum predictions as a function of the interaction strength using an eigenvector continuation emulator applied to the ultracold two-body system introduced in Sec. 2.1. We predict the energy spectrum for both the attractive ($\tilde{g} < 0$) and repulsive ($\tilde{g} > 0$) regime. In addition, we perform an extensive analysis regarding the performance of the emulator and its dependence on the choice of training data. As a result, we propose an algorithm for finding the optimal set of training data and measure the emulator performance using K-fold cross validation.

4.1 Energy spectrum emulations

The implementation and construction of EVC emulators is quite straight forward following the theory presented in Ch. 3, and can be split up into the following steps:

1. Solve the Schrödinger equation in (2.44) for some set of interaction strengths using *exact diagonalization* (ED). This set is denoted the *training points* (tp) $\tilde{g}_{\text{tp}} = \{\tilde{g}^i_{\text{tp}}\}_{i=1}^m$, where m is the number of used training points. In this study, we solve the N-dimensional eigenvalue problem using *Lanczos algorithm* by exploiting the `SciPy` method `eigsh`[1] [14], which is based on the *ARPACK Software* [27].
2. Choose the *training vectors*, i.e. a set of ED eigenvectors corresponding to the training points. Note once again, that we can choose eigenvectors from different excited states for the training points $\tilde{g}_{\text{tp}}$. Recall that the number of training vectors is denoted d, yielding $m \leq d$.
3. Construct the X matrix using the training vectors according to (3.4).
4. Calculate the norm matrix $\mathcal{N}$ (3.10).
5. Calculate the subspace projected Hamiltonian matrices, $\tilde{H}_0$ and $\tilde{H}_1$ (3.14). Construct a set of interaction strengths, the *target values* $\tilde{g}_{\text{evc}}$ where emulated energy values are desired and use $\tilde{H}_0$ and $\tilde{H}_1$ to calculate $\tilde{\mathcal{H}}(\tilde{g})$ for $\tilde{g} \in \tilde{g}_{\text{evc}}$.
6. Solve the generalized eigenvalue problem in (3.8) for the target values to obtain $\tilde{E}(\tilde{g})$ and $\vec{\beta}(\tilde{g})$ for $\tilde{g} \in \tilde{g}_{\text{evc}}$. In this study, we use the `scipy` method `eigh`[2] to solve the generalized eigenvalue problem [14].

[1] The documentation of the method is found at:
`https://docs.scipy.org/doc/scipy/reference/generated/scipy.sparse.linalg.eigsh.html`

[2] The documentation of the method is found at:
`https://docs.scipy.org/doc/scipy/reference/generated/scipy.linalg.eigh.html`

The accuracy of the emulator predictions is measured by comparing the predicted energy spectrum with the spectrum obtained from ED. Hence, we introduce the relative energy error

$$\mathcal{E}_i(\tilde{g}) \equiv \frac{E_i(\tilde{g}) - \tilde{E}_i(\tilde{g})}{\left|E_i(\tilde{g})\right|}, \tag{4.1}$$

where i denotes the energy level. Recall that E is the ED energy obtained by solving the numerical Schrödinger equation (2.44), while $\tilde{E}$ denotes the predicted energy (Ritz value). Due to the variational principle, defined in (3.7), the predicted energy $\tilde{E}_i$ cannot be more accurate than the ED energy, but instead $\tilde{E}_i \leq E$. This means that the numerator in (4.1) is always greater than or equal to zero. Further, the reason why the denominator contains the absolute value of E_i, is to ensure that the relative energy error always remains positive, even for negative energies. The analytical energy solution is plotted in some figures below, and is calculated by solving the transcendental equation (2.33).

4.1.1 Predictions of the ground state energy

In Fig. 4.1 the ground state energy predictions as a function of the interaction strength using two EVC emulators are presented. The emulators are constructed using the ground state eigenvectors for $\tilde{g}_{\text{tp}} = \{1, 2, 3\}$ (orange) and $\tilde{g}_{\text{tp}} = \{-1, -2, -3\}$ (green), respectively. The circles and the solid lines correspond to the training points and the predictions of each emulator. The blue solid dots correspond to $E_0(\tilde{g})$, calculated with ED using $N = 5 \times 10^4$ basis states, while the black dashed line corresponds to the analytical energy.

Note that when using $\tilde{g}_{\text{tp}} = \{1, 2, 3\}$, the extrapolated emulations in the repulsive regime coincide perfectly with the ED values, as shown in the inset. However, the emulator struggles with reproducing the ED results in the attractive regime. The energy difference between the emulator predictions (orange line) and the ED solutions (blue points) grows quite rapidly as g become more negative. In contrast, using $\tilde{g}_{\text{tp}} = \{-1, -2, -3\}$ results in a much more accurate extrapolation in the attractive regime. In addition, the extrapolation to the repulsive regime reproduces the overall shape of $E_0(\tilde{g})$ well. However, in the inset we note that the emulator predictions (green line) do not coincide with the ED values (blue points) as well as the first emulator predictions (orange line) did.

When comparing the predictions of the two emulators in Fig. 4.1, we conclude that for a subspace of dimension $d = 3$ with negative training points we are able extrapolate the overall behavior of $E_0(\tilde{g})$ quite well for $\tilde{g} \in [-10, 30]$, i.e. in both the repulsive and attractive regimes. However, in an attempt to understand the difference in performance and accuracy between the two emulators, we visualize the training vectors as wave functions, $\psi(x)$, in relative coordinates x between the two atoms according to (2.45). This is presented in Fig. 4.2, where the ground state wave functions corresponding to $\tilde{g}_{\text{tp}} = \{1, 2, 3\}$ and $\tilde{g}_{\text{tp}} = \{-1, -2, -3\}$ are presented in 4.2(a) and 4.2(b), respectively.

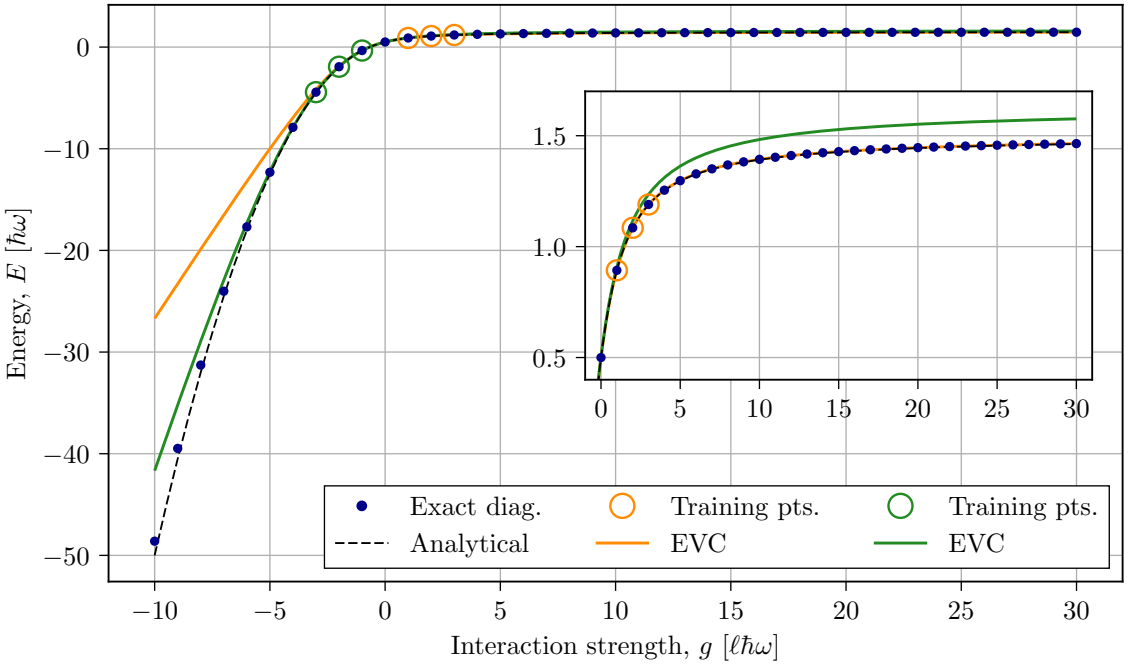

Figure 4.1: Ground state energy predictions from two EVC emulators as a function of the interaction strength g. The emulators are constructed using the ground state wave functions for $\tilde{g}_{\text{tp}} = \{1, 2, 3\}$ (orange) and $\tilde{g}_{\text{tp}} = \{-1, -2, -3\}$ (green), respectively. The inset shows a zoomed-in version of the repulsive regime.

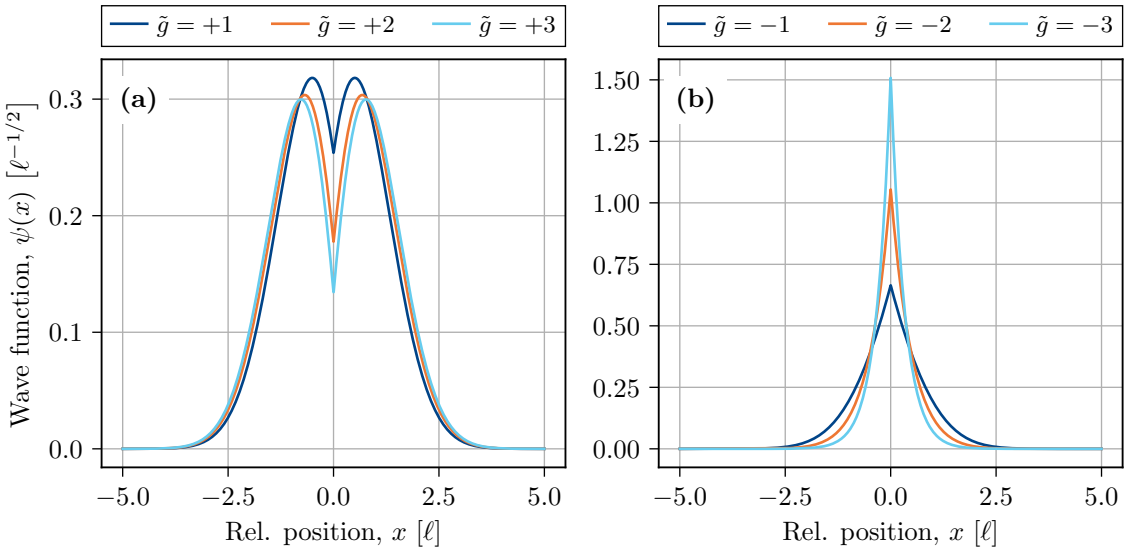

Figure 4.2: The ground state wave functions in relative coordinates for the training points used to construct the emulators in Fig. 4.1. The training vectors from the repulsive and attractive regime are presented in (a) and (b), respectively.

Note the drastically different shape of the ground state wave functions from the two regimes. The coordinate representation of the Ritz vector (3.5) is

$$\tilde{\phi}(x) \equiv \langle x \,|\, \tilde{\phi} \rangle = \langle x | \left(\sum_{i=1}^{d} \beta_i \,|\psi_i\rangle \right) = \sum_{i=1}^{d} \beta_i \sum_{n=0}^{N-1} c_{2n} \,\langle x \,|\, 2n \rangle \overset{(2.45)}{=} \sum_{i=1}^{d} \beta_i \psi(x), \tag{4.2}$$

where $|\psi_i\rangle$ are the training vectors while $\psi(x)$ is the numerical approximation of the wave function (2.45). Thus, $\tilde{\phi}(x)$ becomes a linear combination of the wave functions presented in the figure. This motivates why the extrapolation to the attractive regime when using only three positive training points struggles. The ground state wave functions in the attractive regime have a delta-like shape, which is hard to obtain from a linear combination of the wave functions in 4.2(a). We realize that due to the difference in shape between the wave functions in 4.2(a) and 4.2(b), we need to construct emulators using training vectors from both regimes to enable accurate predictions for the whole interval $\tilde{g} \in [-10, 30]$. Therefore, we use $\tilde{g}_{\text{tp}} = \{-10, 10, 30\}$, i.e. the two extreme values and the middle value of the interaction strength interval. The energy predictions using the new emulator are visualized in Fig. 4.3. Compared to the situation in Fig. 4.1, we now interpolate the eigenvector trajectory instead of extrapolating it. We conclude by looking at the figure that the interpolation predictions capture the overall behavior of $E_0(\tilde{g})$ well. Nonetheless, we notice a quite distinct energy error in the attractive regime for approximately $\tilde{g} \in [-6, -1]$, but the overall performance looks better than in Fig. 4.1.

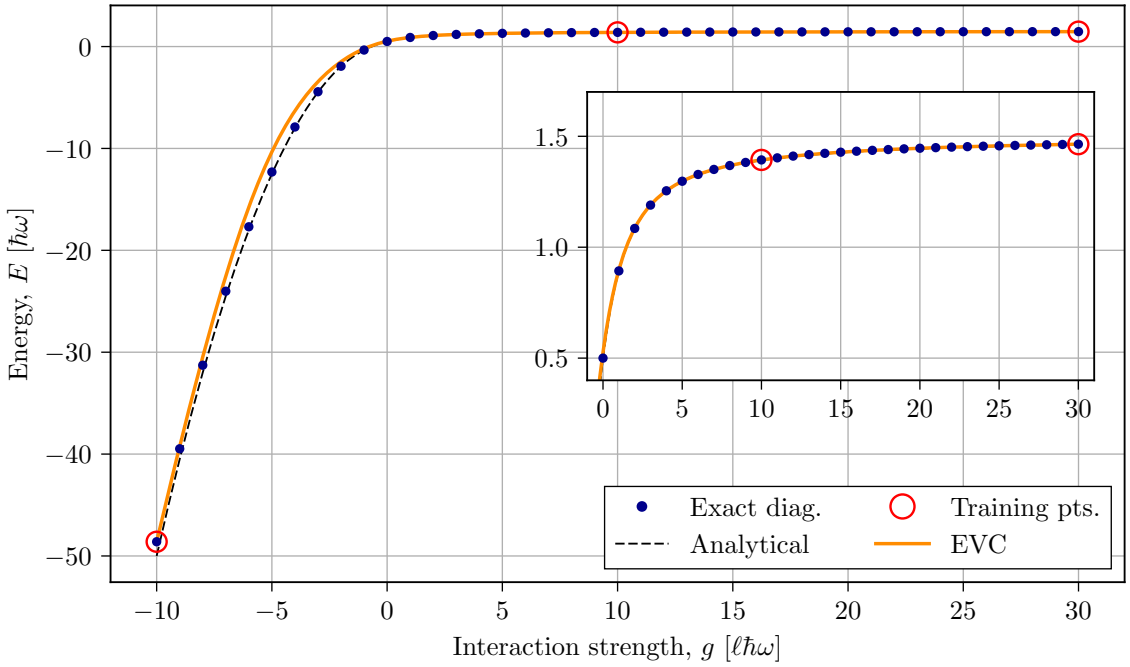

Figure 4.3: Ground state energy predictions from an EVC emulator, with training points $\tilde{g}_{\text{tp}} = \{-10, 10, 30\}$ in the ground state, as a function of the interaction strength g.

The accuracy of the predictions in Fig. 4.1 and 4.3 is displayed as a cross-validation plot with the predicted energy (Ritz value) $\tilde{E}$ plotted against the ED energy E in Fig. 4.4. The accuracy of the predictions is visualized with how much the prediction lines (blue, orange and turquoise) coincide with the $E = \tilde{E}$ line (dashed black line). In the figure we clearly notice that the extrapolation emulations with $\tilde{g}_{\text{tp}} = \{1, 2, 3\}$ is much larger than the ED energies in the attractive regime. We also note that the extrapolation with $\tilde{g}_{\text{tp}} = \{-1, -2, -3\}$ extrapolate well for $\tilde{g} > 0$, however

it also struggles in the attractive regime. Moreover, the interpolation emulations, $\tilde{g}_{\text{tp}} = \{-10, 10, 30\}$, have low accuracy in the attractive regime close to $\tilde{g} = 0$.

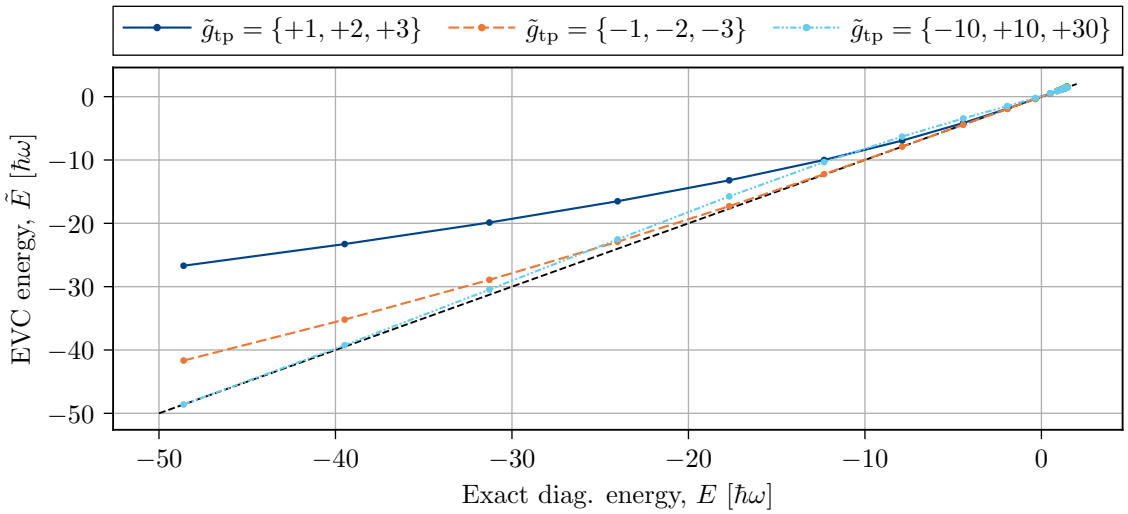

Figure 4.4: Cross-validation plot with the predicted ground state energy (Ritz value) $\tilde{E}_0$ plotted against the ED energy E_0. The straight black dashed line corresponds to $E_0 = \tilde{E}_0$.

An alternative cross-validation plot is presented in Fig. 4.5, with the relative energy error $\mathcal{E}$ (4.1), plotted against the interaction strength g. Due to the logarithmic scale on the y-axis, this figure captures how poor the interpolation emulation (turquoise line) predicts for $\tilde{g} \in [-6, -1]$, with the least accurate prediction for $\tilde{g} = -1$.

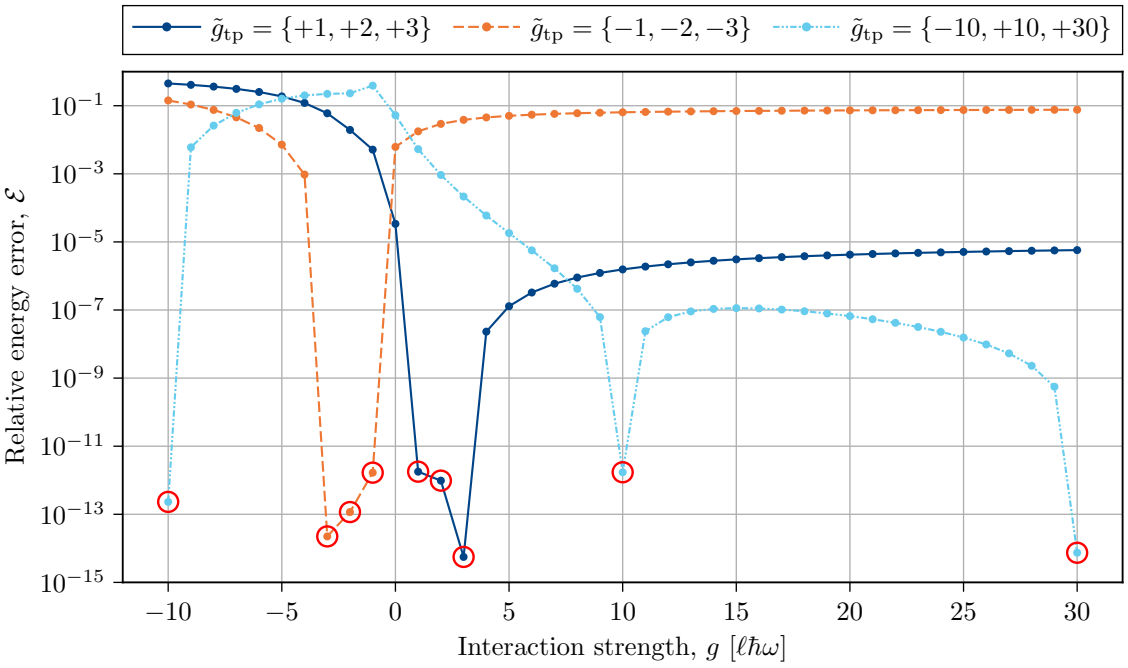

Figure 4.5: Cross-validation of the predictions in Fig. 4.1 and 4.3 with the relative energy error $\mathcal{E}$ plotted against the interaction strength, where the training points are displayed as red circles. Notice the poor accuracy of the interpolation emulation (light blue) for energies in the attractive regime. Furthermore, also note the logarithmic scale on the y-axis.

The overall accuracy can be measure as a *Root Mean Square Error* (RMSE), calculated by taking the square root of the squared energy error sum for the target values $\tilde{g}_{\text{evc}}$. Since we use the relative energy error $\mathcal{E}$, between E and $\tilde{E}$, we denote this measure RMS$\mathcal{E}$, and calculate it according to

$$\text{RMS}\mathcal{E} \equiv \Big(\sum_{\tilde{g} \in \tilde{g}_{\text{evc}}} \big[\mathcal{E}(\tilde{g})\big]^2 \Big)^{1/2}, \tag{4.3}$$

for $\tilde{g}_{\text{evc}} = \mathbb{Z}[-10, +30]$. In Tab. 4.1 the RMS$\mathcal{E}$ values of the predictions in Fig. 4.5 are presented. We notice that the prediction using $\tilde{g}_{\text{tp}} = \{-1, -2, -3\}$ has the lowest RMS$\mathcal{E}$. This is not what we anticipate when comparing Fig. 4.1 and 4.3, where the interpolation emulation seems to capture the overall behavior better. However, this is due to the low accuracy of the prediction for $\tilde{g} \in [-6, -1]$. It is also important to remember that we look at the relative energy error and not the absolute error, which would have given another result. In conclusion, the overall shape of $E_0(\tilde{g})$ is best replicated by the emulator using $\tilde{g}_{\text{tp}} = -10, 10, 30$, however less accurate predictions for $\tilde{g} \in [-6, -1]$ suggest that we should replace the middle training point with $\tilde{g} = -1$, since it is the least accurate prediction in Fig. 4.5.

Table 4.1: The RMS$\mathcal{E}$ (4.3) of the energy predictions in Fig. 4.5 for $\tilde{g}_{\text{evc}} = \mathbb{Z}[-10, +30]$.

$\tilde{g}_{\text{tp}}$	$\{+1, +2, +3\}$	$\{-1, -2, -3\}$	$\{-10, +10, +30\}$
RMS$\mathcal{E}$	0.133	0.065	0.091

To understand why we obtain low accurate predictions in the attractive regime, we visualize the predicted wave functions for $\tilde{g} = \{-8.0, -6.0, -4.0\}$[3] in the relative coordinate in Fig. 4.6. In 4.6(a) the ground state wave functions $\psi(x)$ obtained from ED with $N = 5 \times 10^4$ are presented. Furthermore, in 4.6(b), 4.6(c) and 4.6(d) we visualize the predicted ground state wave functions in relative coordinates $\tilde{\phi}(x)$ (4.2) obtained from emulators using $\tilde{g}_{\text{tp}} = \{+1, +2, +3\}$, $\tilde{g}_{\text{tp}} = \{-1, -2, -3\}$ and $\tilde{g}_{\text{tp}} = \{-10, 10, 30\}$, respectively.

Looking at the ED wave functions in Fig. 4.2, we notice that $\psi_0(x)$ have low densities at $x = 0$ for $\tilde{g} > 0$, while in the attractive regime it exhibits a maximum at $x = 0$. Hence, when comparing $\psi(x)$ with $\tilde{\phi}(x)$ in Fig. 4.6, we notice that the emulator with $\tilde{g}_{\text{tp}} = \{1, 2, 3\}$ are not able to replicate the delta-like shape of the requested wave functions. Furthermore, the wave functions in 4.6(b) reaches only $\sim 2\,\ell^{-1/2}$, while the ED wave function reaches $\sim 4, 3, 2\,\ell^{-1/2}$, for the different interaction strengths. Furthermore, in 4.6(c) we notice that the prediction for $\tilde{g} = -4.0$ (turquoise line) replicates $\psi_0(x)$, while the prediction for $\tilde{g} = -6.0$ (orange line) and $\tilde{g} = -8.0$ (blue line) does not yield the same magnitude as $\psi_0(x)$. This is due to the nearby location of $\tilde{g} = -4.0$ with the training points $\tilde{g}_{\text{tp}} = \{-1, -2, -3\}$, and that the emulator struggles to extrapolate the eigenvector trajectory further than for $\sim \tilde{g} = -4.0$.

[3] Also, none of those points were used as training points in the three emulators.

Comparing this to the result in 4.6(d), where the emulator prediction replicates the shape of $\psi_0(x)$ well for $\tilde{g} = -8.0$, while the prediction for $\tilde{g} = -4.0$ instead exhibit a "smeared-out" shape.

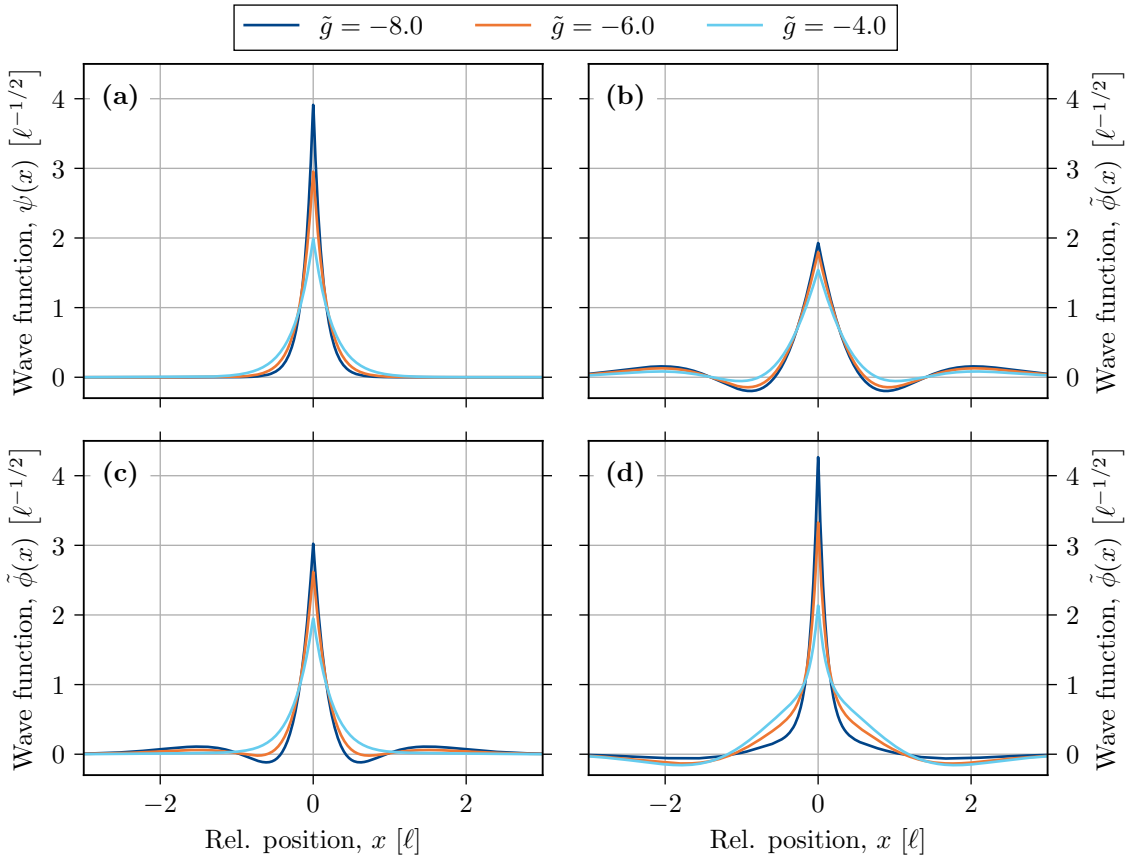

Figure 4.6: The wave functions in the relative coordinate for $\tilde{g} = \{-8.0, -6.0, -4.0\}$. (a) the ED wave functions, while in (b), (c) and (d) the obtained Ritz vectors, expressed as wave functions in relative coordinates, using $\tilde{g}_{\text{tp}} = \{+1, +2, +3\}$, $\tilde{g}_{\text{tp}} = \{-1, -2, -3\}$ and $\tilde{g}_{\text{tp}}\{-10, 10, 30\}$, respectively.

Therefore, we conclude that to get good predictions in the entirety of the attractive regime for $\tilde{g} \in [-10, 0]$, we need to interpolate. To elaborate, we need to mix delta-shaped wave functions with different height in order for the subspace projected prediction to exhibit a delta-like shape as well with a new different height. We do not seem to experience a similar problem in the repulsive regime, since in Fig. 4.5 we see that the predictions become extremely accurate for $\tilde{g} \in [4, 30]$ with $\mathcal{E} < 10^{-5}$ when using $\tilde{g}_{\text{tp}} = \{+1, +2, +3\}$. This once again indicates that in order to construct a more accurate emulator, we should replace the middle training point with one in the attractive regime. As discussed earlier, we replace $\tilde{g} = 10$ with $\tilde{g} = -1$.

The energy emulations with $\tilde{g}_{\text{tp}} = \{-10, -1, 30\}$ are presented in Fig. 4.7. We notice immediately that the predictions in the attractive regime become more accurate. The predicted energy (orange line) coincide perfectly with the ED energies (blue points) in the repulsive regime, while the predictions in the attractive regime look much more accurate compared to before. We conclude that the predicted behavior

of $E_0(\tilde{g})$ is the most accurate so far, with RMS$\mathcal{E} = 0.024$ for $\tilde{g} \in \tilde{g}_{\text{evc}} = \mathbb{Z}[-10, 30]$. This is a significant improvement in accuracy compared to the values obtained in Tab. 4.1.

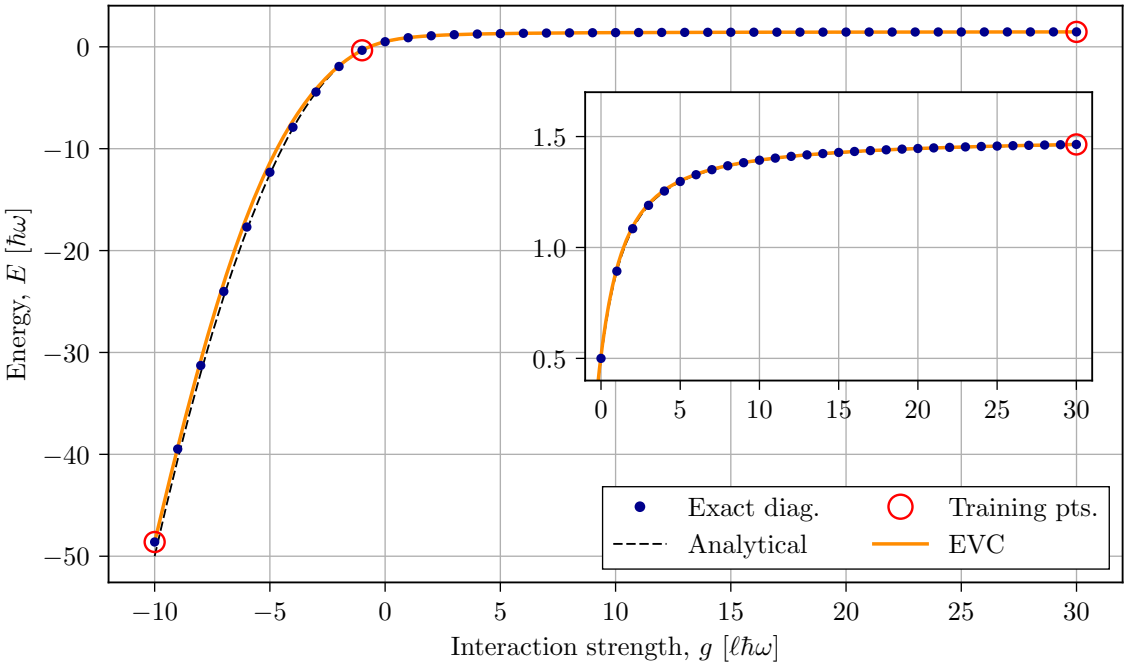

Figure 4.7: Ground state energy predictions as a function of the interaction strength g obtained from an EVC emulator constructed using the ground state wave functions from $\tilde{g}_{\text{tp}} = \{-10, -1, +30\}$ as training vectors.

In conclusion, these four simple emulators illustrate:

- That the EVC emulators predict $E_0(\tilde{g})$ extremely well using only $d = 3$ training vectors, especially the emulator with $\tilde{g}_{\text{tp}} = \{-10, -1, 30\}$ in Fig. 4.7.
- Interpolating the eigenvector trajectory yields more accurate predictions and than when extrapolating. Interpolation is especially needed in the attractive regime.
- How well the extrapolation works, heavily depends on the training points and into which region we extrapolate. Using only three training points in the repulsive regime is enough to extrapolate the behavior of $E_0(\tilde{g})$ extremely well for $\tilde{g} > 0$.
- The overall performance and accuracy of the emulators heavily depends on the choice of training vectors.

The reason why only $d = 3$ training vectors have been used to construct the emulators so far, is to really emphasize the performance using a *few* full solutions. The accuracy will increase if we use more training vectors. Furthermore, in terms of the computational profit, we have reduced the 5×10^4-dimensional eigenvalue problem (2.44), to the extremely small 3×3 generalized eigenvalue problem (3.8) by utilization EVC.

4.1.2 Predictions of the excited state energy

Now we utilize EVC to predict more than just the ground state energy. As such, we aim to predict the low-lying levels of the energy spectrum as a function of the interaction strength. Recall that the size of the generalized eigenvalue problem (3.8) depends on the number of training vectors. This means that if we use d training vectors we obtain d Ritz values, i.e. $\{\tilde{E}_i\}_{i=0}^{d-1}$, with corresponding eigenvectors $\{\vec{\beta}_i\}_{i=0}^{d-1}$ of length d when solving the generalized eigenvalue problem. Thus, we approximate the d lowest energy levels and the corresponding wave functions according to

$$E_i(\tilde{g}) \approx \tilde{E}_i(\tilde{g}), \qquad |\psi_i(\tilde{g})\rangle \approx |\tilde{\phi}(\tilde{g})\rangle = X\vec{\beta}_i(\tilde{g}), \qquad \text{for} \quad i = 0, 1, \ldots, d-1. \quad (4.4)$$

Thus, the number of requested energy levels specify to lower limit of the number of training vectors d.

In Fig. 4.8 the predictions of the three lowest-lying energy levels are plotted as function of the interaction strength. The emulator is constructed using ground-sate wave functions from evenly spaced training points, $\tilde{g}_{\text{tp}} = \{-5, 5, 15, 25\}$, as training vectors. In the figure, we notice that the emulator is able to accurately predict the behavior of the ground state energy $E_0(\tilde{g})$, just as in the previous section. Furthermore, the predictions of the first excited energy level $E_1(\tilde{g})$ is also quite accurate, even though it lies just above the ED energies (blue points) in the repulsive regime. In conclusion, it captures the shape of $E_1(\tilde{g})$ well. However, the emulation of the second excited state does not conform well with the ED energies, especially not in the repulsive regime. Also worth mentioning is that $E_3(\tilde{g})$ lies far above the upper energy limit on the y-axis off and is hence not visible in the figure. To summarize, it appears that the EVC emulator can be used to predict both $E_0(\tilde{g})$ and $E_1(\tilde{g})$ when ground state eigenvectors are used as training data.

Previously, all emulators have been constructed using only ground state eigenvectors as training data. Now we try to enhance the emulators in an attempt to increase the accuracy of the excited energy level predictions. Therefore, we utilize eigenvectors from exited states as training vectors. The result of this is presented in Fig. 4.9, where the emulator is extended with the training vectors corresponding to the second excited eigenvectors for the same training points. This means, that we use the same training points in both the ground and the second excited state, which is visualized once again with read circle in the figure. Now we notice that the emulator is able to predict the behavior of $E(\tilde{g})$ very well for the ground state up to the third excited state, and also quite well for the fourth excited state. This is impressive, considering we only use $d = 8$ training vectors.

It is also worth mentioning that since we only use four training points, namely $\tilde{g}_{\text{tp}} = \{-5, +5, +15, +25\}$, but $d = 8$ training vectors, we only need to solve the eigenvalue problem in (2.44) for the three lowest energy eigenvalues and corresponding eigenvectors for four different values of $\tilde{g}$ when using the Lanczos algorithm. If we want to add excited eigenstates as training vectors, we need to solve the eigenvalue problem for all lower lying eigenstates first[4]. This means that

[4] At least without having to modify the Hamiltonian matrix first.

using the same training points for different excitations is the most efficient in regards of computational powers.

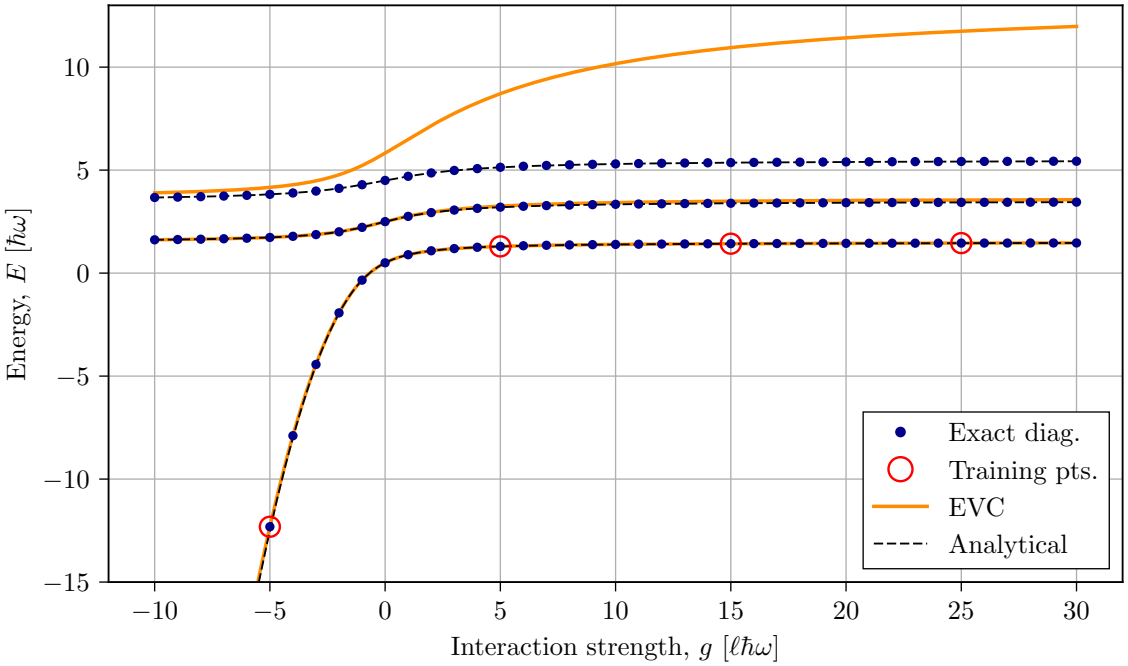

Figure 4.8: The predictions of the three lowest-lying energy levels as a function of the interaction strength. The emulator is constructed using ground-sate eigenvectors from evenly spaced training points, $\tilde{g}_{\text{tp}} = \{-5, 5, 15, 25\}$, as training vectors.

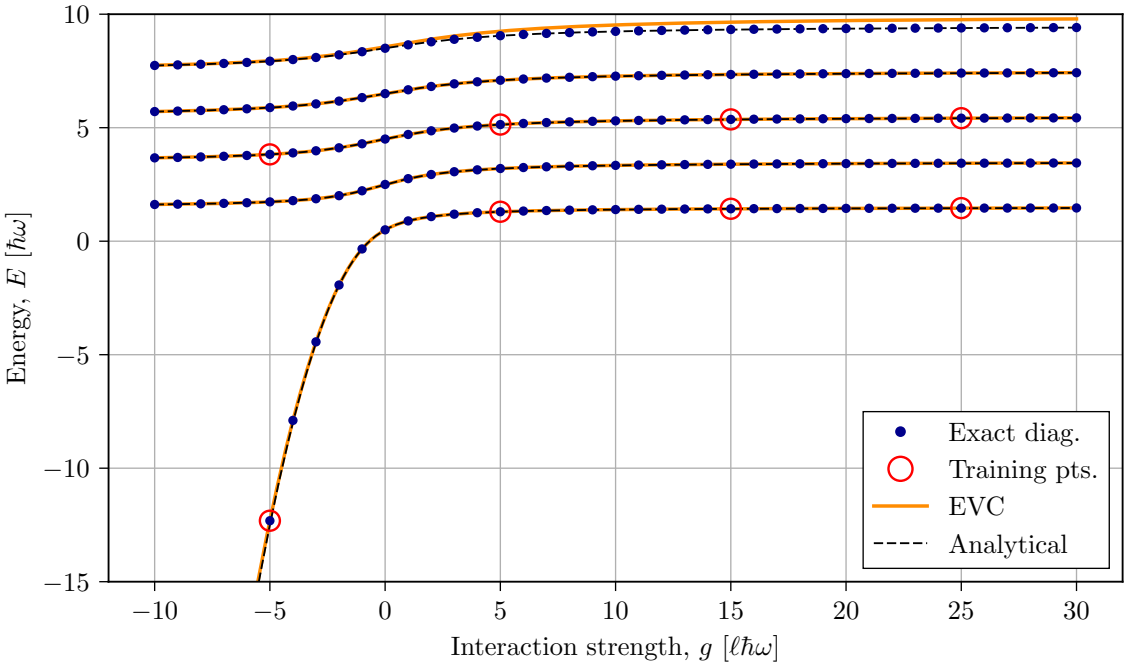

Figure 4.9: Prediction of the five lowest energy levels as a function of the interaction strength using an EVC emulator constructed with the ground- and second excited state eigenvectors as training vectors, for the training points $\tilde{g}_{\text{tp}} = \{-5, 5, 15, 25\}$.

In Fig. 4.10 we present the cross-validation of the predictions in Fig. 4.9. The relative energy error $\mathcal{E}$ for the different energy levels is plotted against the interaction strength. Note that it is plotted in a wider regime, namely $\tilde{g} \in [-100, 100]$, and we obtain an overall great accuracy. However, the accuracy of $\mathcal{E}_0(\tilde{g})$ for $\tilde{g} < 0$ (dark blue line) is still quite low, while the accuracy of the excited state energy predictions in the attractive regime is extremely high. The emulation accuracy of $E_1(\tilde{g})$, $E_3(\tilde{g})$ and $E_4(\tilde{g})$ are even higher in the attractive regime compared to the repulsive regime. This is contrary to the ground state predictions, and probably has to do with the fact that the excited state wave functions in the attractive regime have a similar shape as the wave function functions of one lower exited state in the repulsive regime. Hence, the eigenvector trajectory for the ith excited state in the attractive and the $i-1$th state in the repulsive regime is continuous in $\tilde{g} = \infty$ and $\tilde{g} = -\infty$, thus enabling extrapolation between these excitations. This is probably the reason why we have such high accuracy for the predictions of $E_1(\tilde{g})$ and $E_3(\tilde{g})$ for $\tilde{g} < 0$, since we use three training points from the ground and second excited state each in the repulsive regime.

To summarize, we conclude that we obtain extremely accurate predictions of the low-lying energy spectrum for the ultracold two-body system for $\tilde{g} \in [-100, +100]$ when using excited state wave functions as training vectors. Unfortunately, there is a limitation with adding more training vectors. For example, when adding the fourth excited state wave functions for the same training points as in Fig. 4.9, the condition number of the norm matrix $\mathcal{N}$ become too large, and the generalized eigenvalue problem becomes numerically unstable. Just as we discussed in Ch. 3, this means that the training vectors are almost linearly dependent. Therefore, we must choose the training vectors carefully since we cannot just keep adding full solutions with the expectation of persistently increasing the accuracy of the emulations.

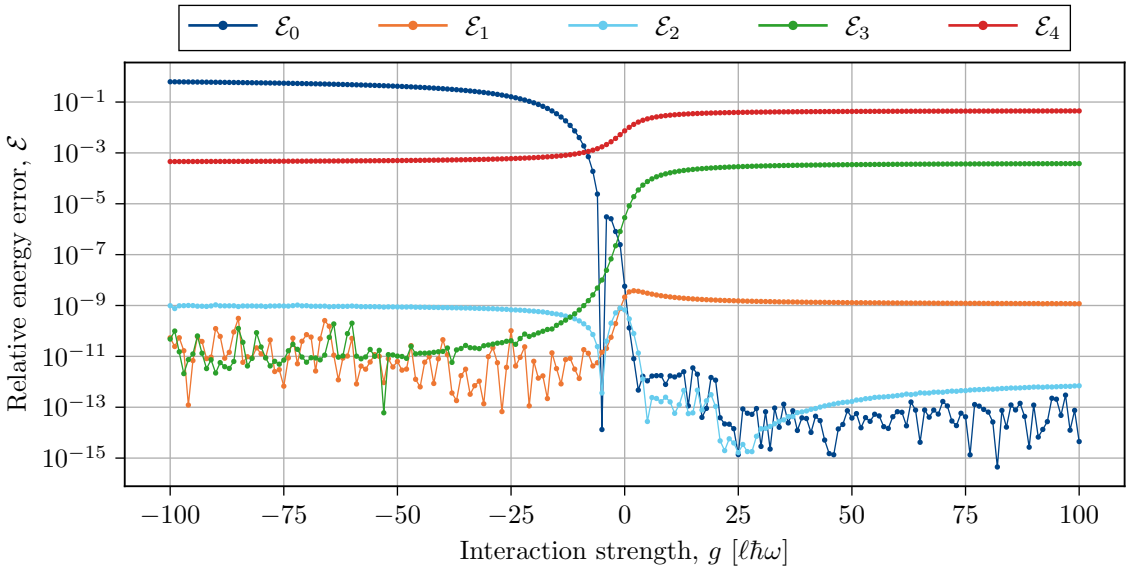

Figure 4.10: Cross-validation of the predictions in Fig. 4.9 with the relative energy error $\mathcal{E}$ for the five lowest lying energy levels, plotted against the interaction strength. Notice that the x-axis contains a wider regime than before, namely $\tilde{g} \in [-100, 100]$.

So far, in this section, we conclude that the selection of the training points plays a crucial part in the performance and accuracy of the EVC emulators. Unfortunately, we are also faced with a dilemma: ill-conditioned norm matrices. This means that we cannot just keep adding more and more training vectors—the condition number will eventually become too large. Also, in regards of the computational power, we want to use as few training vectors as possible. Thus, we want to find a way of choosing the optimal training points without venture the risk of obtaining an ill-conditioned norm matrix.

4.2 Optimal training vector algorithm

In this section, we aim to find a way to choose an optimal set of training vectors. We propose the overlap between the Ritz vector and the ED eigenstate, i.e. $|\langle\psi(\tilde{g})\,|\,\tilde{\phi}(\tilde{g})\rangle|^2$, as a measure to determine an optimal set of training vectors. When the overlap is equal or close to one, it means that the obtained Ritz vector is a great approximation of the actual eigenstate. In that case, the requested state primarily lies within the subspace S (3.3). When the overlap is small, however, it means the opposite.Therefore, we want to add new training vectors where the overlap is small. The algorithm outlined below does exactly that. The prerequisite for running the algorithm is to have a set of calculated eigenvalues with corresponding eigenvectors for multiple interaction strengths, which are denoted *available points* with the abbreviation $\tilde{g}_\mathrm{a}$. Thus, we introduce the *optimal training vector algorithm*:

Optimal training vector algorithm

Choose the first training point $\tilde{g}_1 \in \tilde{g}_\mathrm{a}$ as:
The negative value of $\tilde{g} \in \tilde{g}_\mathrm{a}$ closest to $\tilde{g} = 0$

The algorithm for choosing the next training point:

1. Create an EVC emulator utilizing the ground state eigenvector for $\tilde{g}_\mathrm{tp} = \{\tilde{g}_k\}_{k=1}^{i}$ as training vectors, where i denotes the number of added training points so far.
   - Calculate RMS$\mathcal{E}$ for $\tilde{g} \in \tilde{g}_\mathrm{test}$.
   - Calculate the overlap between $|\tilde{\phi}\rangle$ and $|\psi\rangle$ for $\tilde{g} \in \tilde{g}_\mathrm{a}$, i.e. $|\langle\tilde{\phi}(\tilde{g})\,|\,\psi(\tilde{g})\rangle|^2$. It is important that the Ritz vector is normalized.
2. Choose the $\tilde{g} \in \tilde{g}_\mathrm{a}$ with the lowest overlap, i.e.

   $$\tilde{g}_{i+1} = \underset{\tilde{g}\in\tilde{g}_\mathrm{a}}{\operatorname{argmin}} |\langle\tilde{\phi}(\tilde{g})\,|\,\psi(\tilde{g})\rangle|^2 \,.$$

3. Repeat 1 and 2 until desired dimension d of the subspace S.

In the following, the performance of this algorithm is validated using a 20/80 shuffled K-fold cross-validation. We have calculated the eigenvalues and ground state eigenvectors for integers values of $\tilde{g}$ between -100 and $+100$ using exact diagonalization, with $N = 1 \times 10^4$ (in contrast to $N = 5 \times 10^4$ used previously). Therefore, the train-test-split yields 40/41 available points ($\tilde{g}_{\text{a}}$) and 161/160 test points ($\tilde{g}_{\text{test}}$). The calculated values are shuffled randomly and then split into five different sets. In the first cycle, the first set will be the available points, while the remaining four sets will constitute the test points. In the next cycle, the second set will be the available points while the remaining four will constitute the test points, and so on for a total of five cycles. In every cycle, we use the algorithm for constructing the EVC emulator and stop at $d = 12$ chosen training points. In every step, we use the emulator to predict the ground state energy for $\tilde{g} \in \tilde{g}_{\text{test}}$ and calculate the corresponding RMS$\mathcal{E}$ for the five lowest energy levels. However, it is important to notice that we cannot obtain more energy level predictions than the number of training vectors. This means that in the first iteration we can only predict the ground state energy, and in the second iteration we can only obtain the ground and first excited state energies and so on. Thus, it is not until the fifth iteration that we obtain all five requested energy predictions.

Therefore, when we have used the algorithm for all $K = 5$ cycles in the K-fold cross-validation, we have obtained five RMS$\mathcal{E}$ values for every energy level. The train-test-split is then repeated, and we do the same K-fold cross-validation procedure once again. In total, we perform the train-test-split 100 times, yielding a total of 500 RMS$\mathcal{E}$ values for every step in the algorithm. The results are presented in Fig. 4.11, where the RMS$\mathcal{E}$ is plotted against the number of training points d used to construct the emulator. The solid lines correspond to the median of the 500 RMS$\mathcal{E}$ values for the five lowest energy levels, and the filled areas correspond to the 68% and 95% highest density interval (HDI).

The demonstrated performance shown in Fig. 4.11 could be used to decide how many training points to use in order to achieve a desired accuracy. In the figure, we notice that the RMS$\mathcal{E}$ for the exited states are in general much larger, which is anticipated since we only add ground state wave function as training vectors in this algorithm. We conclude that when using only $d = 10$ training vectors all of the 90% HDI is below a RMS$\mathcal{E}$ value of 10^{-3}, which is an incredible prediction accuracy, especially considering we only solve a 10-dimensional generalized eigenvalue problem (3.8). In addition, we obtain really high accuracy of both the first and second excited state energies as well, with median RMS$\mathcal{E}$ values around 2×10^{-3} and 1×10^{-1}, respectively, for $d = 12$.

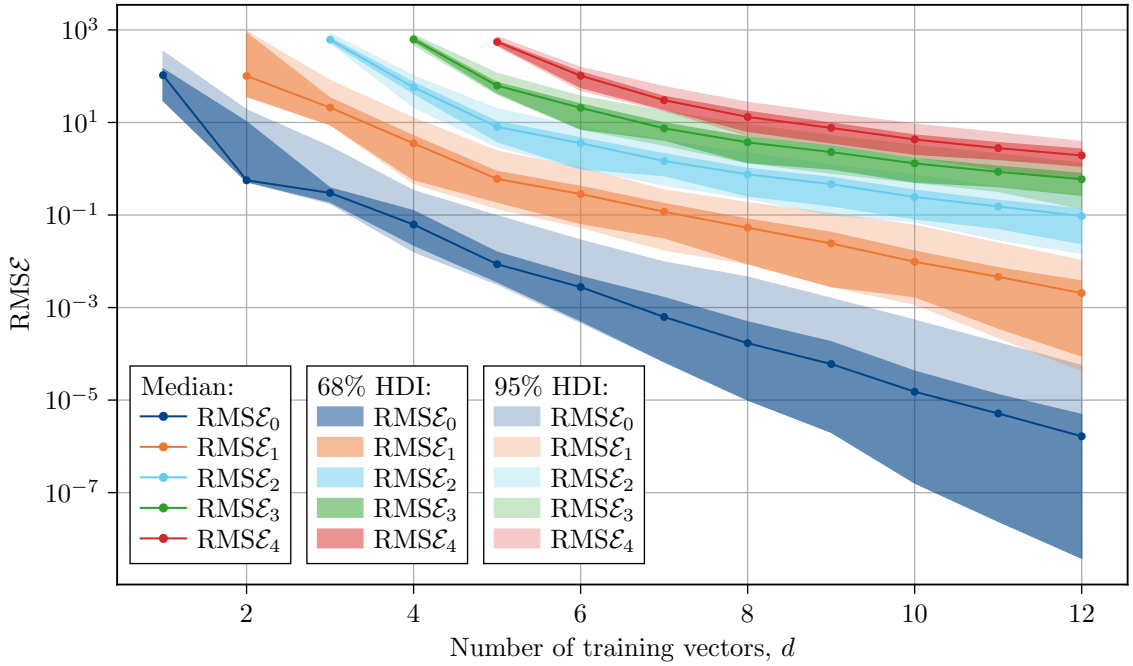

Figure 4.11: The performance of the *Optimal training vector algorithm* with the RMS$\mathcal{E}$ of the test sets plotted against the number of training vectors d. The solid dots correspond to the median RMS$\mathcal{E}$ value of all runs, and the dark (light) filled areas correspond to the 68% (95%) highest density interval for the five lowest energy levels.

A normalized histogram of all the training points were selected during the K-fold cross validation runs is presented in Fig. 4.12. Notice that the simple algorithm suggests that we obtain more accurate predictions when we interpolate the eigenvector trajectory, rather than extrapolating it. Also, note that a significant majority of the training points are from attractive regime.

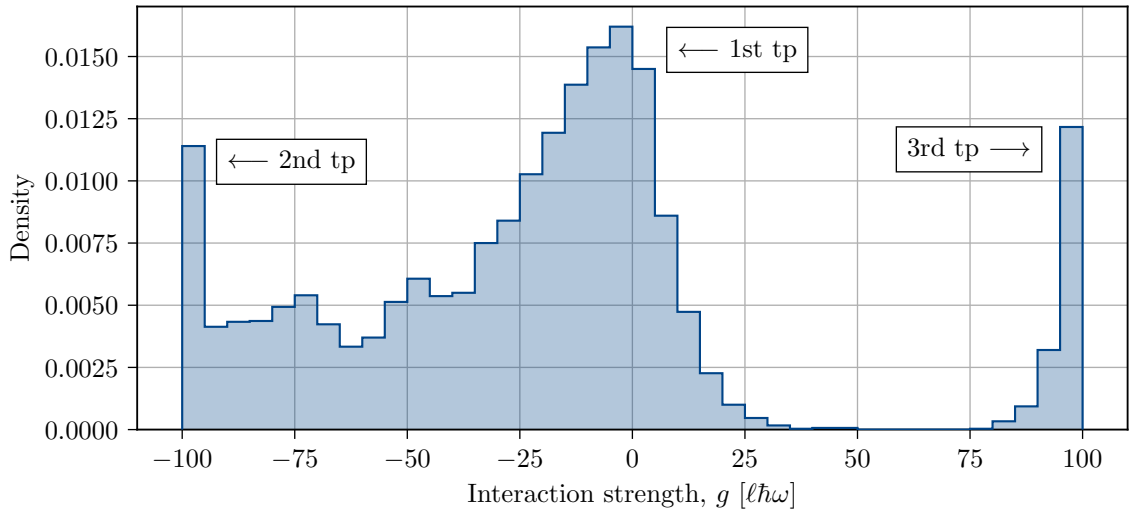

Figure 4.12: A normalized histogram of all the training points picked during the K-fold cross validation runs.

Furthermore, we investigate in which general order the algorithm added the selected training points to the emulator. Apart from the fixed starting point $\tilde{g}_1$, we find that the first (second) selected point is $\tilde{g}_2 = \min\{\tilde{g}_\mathrm{a}\}$ ($\tilde{g}_3 = \max\{\tilde{g}_\mathrm{a}\}$), hence the peak around $\tilde{g} = -100$ ($\tilde{g} = +100$) in Fig. 4.12. Also, note the almost no training points is selected in the regime $\tilde{g} \in [20, 80]$. This suggest that the corresponding eigenvectors are similar making them ineffective to use as training vectors. The choice of training points used to construct the emulator for predicting the energy spectrum for the many-body system will be based on the result in this chapter, where we have showed that the interpolation yields more accurate results, but also that most of the training vectors should preferably be eigenstates from the attractive regime.

5. Many-body energy emulations

In this chapter, we construct EVC emulators for the generalized ultracold many-body systems introduced in Sec. 2.2. We present the performance and accuracy of the ground state energy predictions as a function of the interaction strength in both the attractive ($\tilde{g} < 0$) and repulsive ($\tilde{g} > 0$) regime. The systems considered here consist of three (2+1) and five (4+1) ultracold fermionic atoms. The implementation of constructing the emulators is the same as for the two-atomic system described in Ch. 4, however, now we use the code by J. Lindgren [6], [15] to obtain the Hamiltonian matrices, see Sec. 2.2 for details on the setup of the many-body system and solution using exact diagonalization. Recall that the many-body eigenstates are now expressed in a single-particle basis—compared to the relative coordinate basis used for the two-body system in Ch. 4–but that is irrelevant for EVC. Also, the same notations and abbreviations will be used in this chapter. However, one difference is that the energy spectrum is plotted as a function of $-1/g$, instead of g. Therefore, $\tilde{g}^*_{\text{tp}} = \{\tilde{g}_1, \tilde{g}_2, ...\}$ and $\tilde{g}^*_{\text{evc}} = \{\tilde{g}_1, \tilde{g}_2, ...\}$ denotes that $-1/\tilde{g}_1$, $-1/\tilde{g}_2$ etc. are used as training or target points, respectively[1]. In addition, we introduce a notation for a set of evenly spaced $\tilde{g}$-values as [start, end, step size].

We consider the ground state energy evolution for the $2+1$ and $4+1$ systems with both even ($\pi = +1$) and odd ($\pi = -1$) parity. As we mentioned in Sec. 2.2, when constructing the Hamiltonian matrices, we can select if we want to include odd or even (or both) parity states. We have treated the Hamiltonian constructed using even and odd parity states as two different systems, even though the same particle configuration is used. This means that we consider four different systems in this chapter, as presented in Tab. 5.1.

Table 5.1: The many body systems considered in this study with $n_\uparrow$ ($n_\downarrow$) atoms with spin up (down) and total parity π. The many-body basis is constructed with a total energy truncation N_{max} and yield a Hamiltonian matrix of size $N \times N$.

System			Truncations	
$n_\uparrow$	$n_\downarrow$	π	N_{max}	N
2	1	+1	80	22 960
2	1	−1	80	23 821
4	1	+1	35	18 588
4	1	−1	35	21 003

In Sec. 2.1 and Ch. 4, the number of even parity harmonic oscillator basis states N directly translates to the Hamiltonian matrix size. However, now the basis state

[1] The asterisk ($*$) is used to keep this apart from the abbreviation $\tilde{g}_{\text{tp}}$ used in Ch. 4.

truncation is given by $N_{\max}$ instead, which is the total energy quanta cutoff in harmonic oscillator units ($\hbar\omega$). This means that the total energy quanta of the many-body harmonic oscillator states in (2.50) is less than or equal to $N_{\max}$. The combinatorial size of the matrix increases rapidly as $N_{\max}$, or the number of particles, is increased. Therefore, in Tab. 5.1 we show the resulting matrix size N, which is also the dimensionality of the resulting Hilbert space.

We are once again faced with the decision of choosing training points when constructing the emulators. Fortunately, now we have prior knowledge, and we can base our choice on the analysis presented in Fig. 4.12 for the $1+1$ system. There we investigated in which order the points were added by our algorithm when constructing an optimal emulator and found that—apart from the fixed starting point—the first two choices were the extreme points in the two regimes.

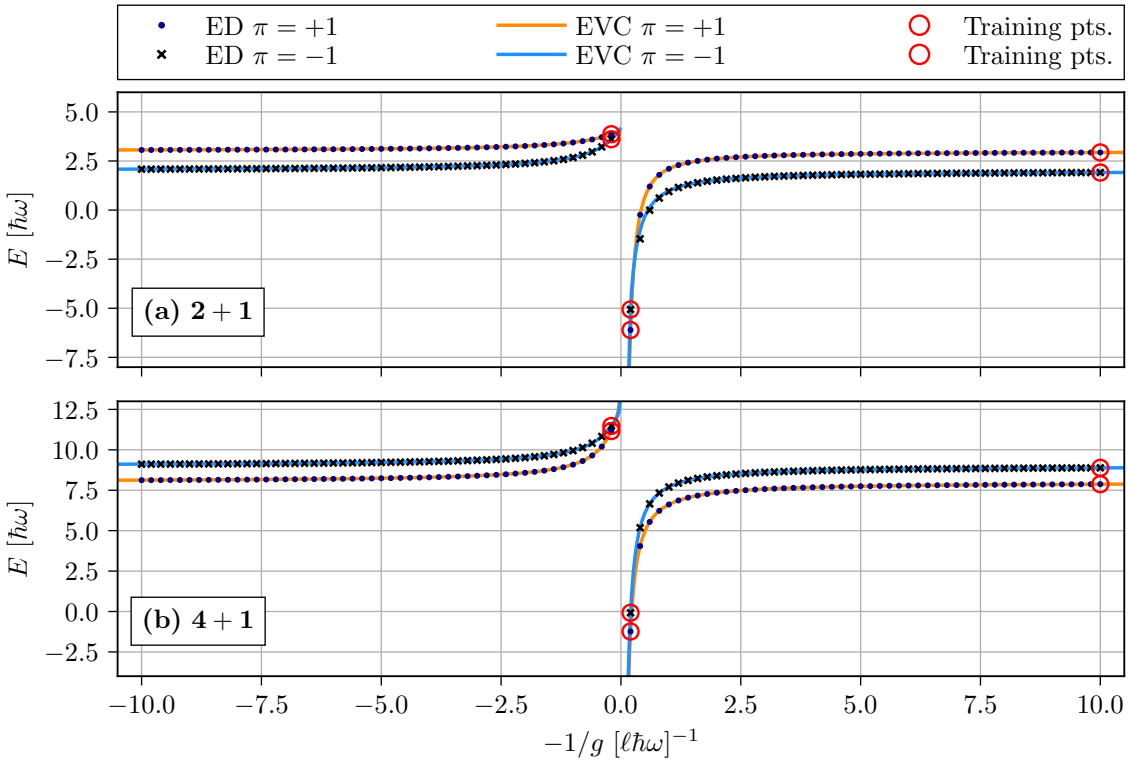

Figure 5.1: The ground state predictions as a function of $-1/g$ using EVC emulators with $\tilde{g}^*_{\text{tp}} = \{+0.2, +10, -0.2\}$.

We have calculated the energies for the $2+1$ and $4+1$ systems, using exact diagonalization in the same way as in Ch. 4 for evenly spaced of the inverse interaction strengths, namely $-1/g \in [-20, 20, 0.1]$. The ground state predictions as a function of $-1/g$ using EVC emulators with $\tilde{g}^*_{\text{tp}} = \{+0.2, +10, -0.2\}$ for the four systems in Tab. 5.1 are presented in Fig. 5.1. The training points corresponds to the extreme points for $-1/\tilde{g} \in [-10, -10, 0.2]$, namely $1/\tilde{g} = \pm 0.2$ and then the third point is chosen analogously to the starting point in our algorithm, i.e. $-1/\tilde{g} = 10$.

Also, note that all emulators are constructed using the same training points[2].

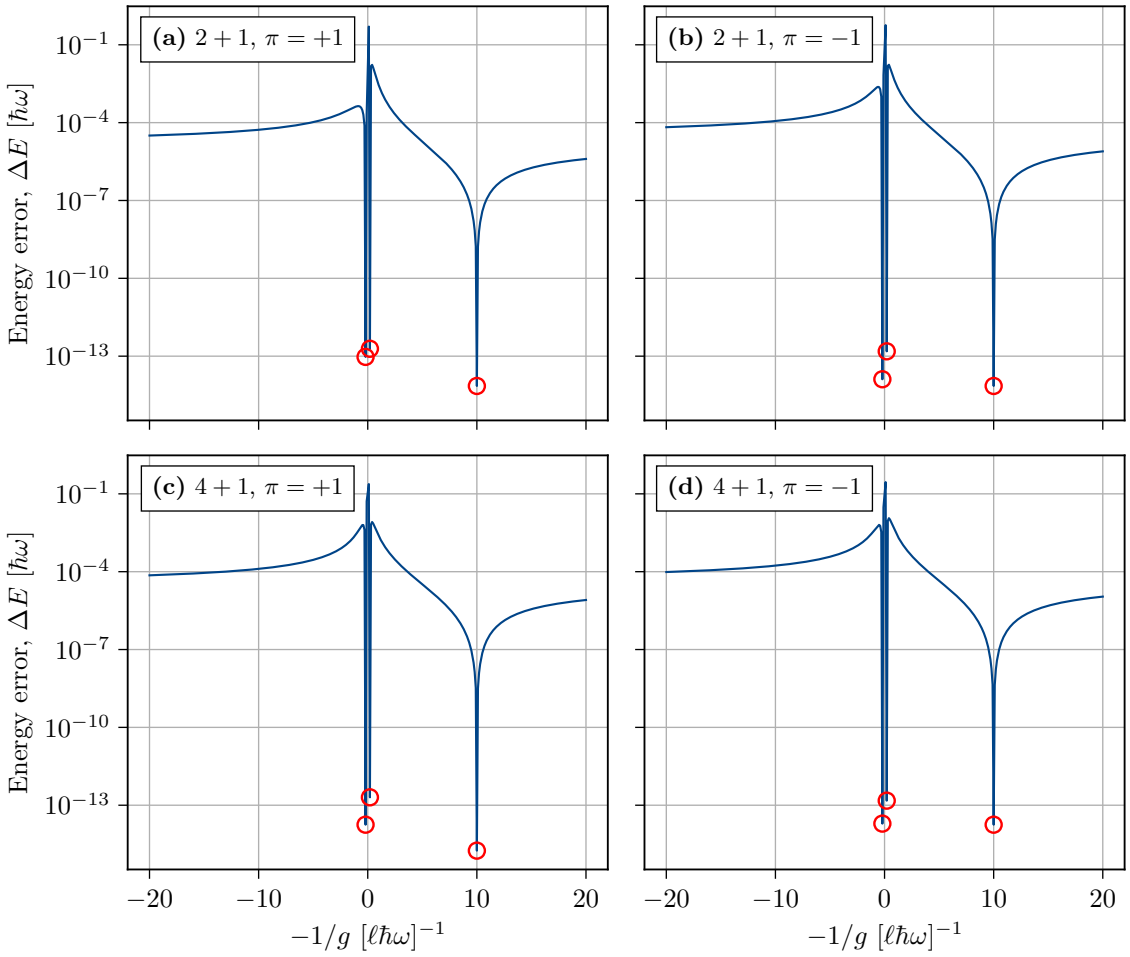

Figure 5.2: Cross-validation of the predictions in Fig. 5.1 with the ground state energy error $\Delta E = \tilde{E}_0 - E_0$ plotted against $-1/g$. In (a), (c) and (d), for $-1/g = 10$ the energy error is negative, and we have therefore plotted the absolute value at these three points instead. The reason why it does not satisfy the variational principle (3.7) in these points, is probably due to machine precision error.

In Fig. 5.1 we notice that the emulated energies coincide perfectly with the ED energies when using only three training vectors. Visually, the accuracy of the emulations looks even better than the result for the $1+1$ system shown in Fig. 4.7. Again, we use cross-validation to measure the accuracy of the emulations. This accuracy study of the predictions in Fig. 5.1 is presented in Fig. 5.2. The ground state energy error, $\Delta E = \tilde{E}_0 - E_0$, is plotted against $-1/g$, in the wider regime $-1/g \in [-20, 20, 0.1]$ since we want to investigate and measure the difference between extrapolating and interpolating the eigenvector trajectory. Thus, we compare emulator performance for interpolation ($|\frac{1}{g}| < 10$) and extrapolation ($|\frac{1}{g}| > 10$). Furthermore, we also extrapolate from $-1/g = 0.2$ (-0.2) to $-1/g = 0.1$ (-0.1). Most of the points with lower relative error than 10^{-3} is the interpolation

[2] But of course with different eigenvectors as training data.

for $|1/g| < 0.2$ (-0.2), contributing to the peaks around $-1/g \approx 0$ in Fig. 5.2 and for all systems, the maximum occurs for $-1/g = 0.1$. Thus, we conclude that also the many-body emulators struggle with extrapolation to the strongly attractive regime. However, looking at the figure, we notice an overall excellent accuracy with relative errors less than 10^{-3} for 98 % of the total points.

In Tab. 5.2 we present the RMSE[3] values calculated from the result in Fig. 5.2, where we sum of the square of the errors for $\tilde{g} \in \tilde{g}_{\text{evc}} = [-20, +20, 0.1]$. It is difficult to compare the accuracy of these prediction with the predictions in Ch. 4, since the energy emulations are performed for different interaction strength intervals. However, given the energy scale that is involved we can conclude that we are able emulate the evolution of $E(-1/g)$ with high accuracy for all systems in Tab. 5.2 using only three training points. In addition, we notice that the accuracy is quite significantly higher for the $4+1$ systems compared to the $2+1$ systems. This result suggests that the accuracy of the ground states energy predictions does not decrease as the number of particles, and hence the complexity of the wave functions increases.

Table 5.2: The RMSE of the predicted energy in Fig. 5.2 calculated for $\tilde{g}_{\text{evc}} = [-20, +20, 0.1]$.

System	$2+1$, $\pi = +1$	$2+1$, $\pi = -1$	$4+1$, $\pi = +1$	$4+1$, $\pi = -1$
RMSE $[\hbar\omega]$	0.025	0.029	0.012	0.014

In summary, we conclude that emulators constructed with three training points based on the suggested order in Fig. 4.12 produce extremely accurate predictions for both the $2+1$ and $4+1$ systems. This indicates that the ranking of optimal training points that was identified by our algorithm in the two-body problem, can be successfully applied when constructing emulators for the many-body systems, yielding a completely new dimension of usefulness for the algorithm in Sec. 4.2. This could be of great use when applying the method of EVC to new physical systems in the future by finding the optimal training points for a less complex version of the same system and then use the findings when the complexity and combinatorial size is scaled up. In our case, the algorithm more or less only showed that the EVC emulator yields more accurate predictions when we interpolate, rather than extrapolate. However, the algorithm is probably more useful in more dimensions, i.e. when the Hamiltonian matrix depends on more than one parameter, since it uses the overlap metric to decide on the optimal training points.

A more comprehensive study of the many body emulations would have been needed in order to be certain of this conclusion—comparing different emulators and scaling up the number of particles in the generalized ultracold fermionic system. Unfortunately, this was not within the scope of this project. We still conclude that we obtain extremely accurate predictions of the generalized system with three and five particles using only three training points.

[3] Notice that this is calculated using the absolute error, and not the relative error as in Tab. 4.1. The reason why we do not use the relative error is because $E \approx 0$ at $\tilde{g}^*_{\text{tp}} = 0.2$ for the $4+1$, $\pi = -1$, thus yielding a really large relative error and making $\mathcal{E}$ misleading.

6. Conclusion and outlook

The aim of this study was to describe the evolution of the energy spectrum of trapped systems of ultracold atoms as a function of the tunable interaction strength by utilizing EVC emulators. We have shown that the EVC predictions are very accurate in both the attractive and repulsive regime, even when only using three eigenvectors as training data. We have also proposed an algorithm for finding the optimal set of training data for the two-atomic system and employed our findings with much success, when constructing emulators for predicting the ground state energy of many-body systems with three (2+1) and five (4+1) atoms.

The optimal training points algorithm
The algorithm in Sec. 4.2 dictates how to choose the optimal set of training points from a larger set of precalculated eigenvalues and eigenvectors. Hence, one question arises—how could the algorithm be used in practice when constructing EVC emulators? To answer this, we present three potential applications:

1. In Ch. 5, we discussed the possibility of first applying the algorithm for a less complex, and hence computationally less demanding problem, with the intention of using the findings to choose training points for a scaled-up or generalized version of the same system. We foresee that it could be used similarly for finding the optimal training points for a system with a much smaller basis truncation, i.e. the same system but with Hamiltonian matrices of much lower dimensions. In both these cases, we assume that we can use exact diagonalization more efficiently for the "smaller version" of the systems, and thus use the algorithm in a similar way as in Sec. 4.2. The suggestion would be to use the obtained optimal training points but for the much higher-dimensional version, where exact diagonalization is much more costly. As an example, if we were to use the algorithm for the many-body system in Sec. 2.2 for a smaller value of $N_{\max}$, and then use the obtained result to choose training points for a system with a much larger value of $N_{\max}$.

2. The algorithm can also be used to choose the optimal training points while estimating the accuracy of an EVC emulator. To obtain a measure of the accuracy, one must calculate the energy using exact diagonalization for more points than the training points and construct some validation or test set. Therefore, one has to decide which points that should be used as training points, similar to the situation in Sec. 4.2, where we want to find the optimal set. One would normally pick training points randomly, or try to minimize some kind of summary statistics, e.g. the RMSE value, either by trying all combinations or by applying some type of optimization. This is often performed in machine-learning applications by optimizing training hyperparameters in an artificial neural network to minimize a selected error score. Our algorithm, on the other hand, suggests a way of choosing the optimal training points in a systematic and

well-defined way by selecting points with the minimum overlap. We foresee that this could be of great benefit especially when dealing with systems where the Hamiltonian depends on more than one continuous parameter.

3. Another potential application is to slightly redefine the algorithm in an attempt to find the optimal training points *without* having precomputed eigenvectors to base the selection on. In the modified algorithm one would need to choose some set of initial training points, and then use the algorithm to continuously expand the set of training points. This could be accomplished by utilizing *Bayesian Optimization with Gaussian Processes*, with the intention to model the overlap as a function of the continuous parameter with a Gaussian process—in our case to model $|\langle\tilde{\phi}(\tilde{g})\,|\,\psi(\tilde{g})\rangle|^2$ as function of $\tilde{g}$. Subsequently, define an acquisition function that helps to identify the next point to be added to the set of training points based on the current knowledge of the overlap. By repeating this, one continuously expands the subspace of the emulator with more training points.

In this study we have used ground states as training vectors. However, the algorithm can also be extended to include training vectors from excited energy levels as well. This could be very beneficial if one aims to describe the evolution of several levels in the energy spectrum. It can also help to avoid obtaining an ill-conditioned norm matrix, since there are more eigenvectors to choose from. It would also have been interesting to explore the use of $\tilde{g} = 0$ as a training point, since the eigenvectors are trivially obtained for this case due to the matrix being diagonal. As such, this is a *free* training point, and could perhaps have replaced the current initial point in the algorithm.

More complex and realistic ultracold systems

It would have been interesting to apply the method of EVC to more complex and realistic physical systems with a many-parameter Hamiltonian. One of the main limitations of this project has been that we only considered systems with a single tunable continuous parameter. As mentioned in Ch. 3, the method of EVC can be used to construct emulators for predicting the energy when the Hamiltonian matrix depends on more than one continuous parameter. Thus, it would be interesting to measure the performance of an EVC emulator applied to a more generalized version of the ultracold atomic systems considered in this project. There are several relevant situations with higher-dimensional parameter volumes that can be perceived, and we present three possible cases where EVC emulators could be used to predict the energy as some parameters are varied:

1. One interesting application of EVC would be to predict the energy of systems with interactions both between atoms of different species and between the same species. With such an additional interaction, the $n_\uparrow + 1$ system would contain two different interaction parameters, while an even more general $n_\uparrow + n_\downarrow$ system would contain three. This would increase the complexity significantly and yield a higher demand on the ability of the EVC emulators—with potentially a much higher benefit in terms of computational power. In particular, we foresee that our algorithm could be very useful for this kind of systems since it is much more

difficult to choose training points in higher dimensions. Indeed, the systematic way of finding the optimal set of training vectors could be very useful in this scenario.

2. Furthermore, the zero-range interaction model could be replaced with a more realistic short-range functional form, e.g., a Gaussian potential with mean $\mu = 0$ which would still yield an analytical expression for the interaction matrix elements. The width σ in the Gaussian potential would hence become an additional continuous, though not linear, parameter that could be varied. This would mean that the Hamiltonian matrix would depend on both the height (interaction strength) and width of the Gaussian, making it an interesting system to emulate using EVC.

3. A third application would be to apply EVC to systems with an external *deformed trap potential*, meaning that the external trap potential is not a perfect harmonic oscillator [28]. This would also introduce non-linear continuous parameters to the Hamiltonian matrix that could be varied to tune the shape of the trap.

It is important to note that the Hamiltonian will depend continuously, but not linearly, on many of the parameters discussed above. This is sufficient for EVC application, even though the subspace projection that is required when applying the emulators will be less efficient compared to the case of linear dependent parameters.

Conclusion

With this study, we have shown that the method of EVC can be used to predict the energy eigenvalues of realistic ultracold atomic quantum systems. As such, we have extended the usage of EVC to a new field of physics, where we obtained extremely accurate energy predictions using only three full solutions as training data. EVC emulators could potentially be applied to much more complex ultracold atomic systems with higher-dimensional parameter volumes. Our three examples above illustrate that continuous parameters could appear both in the interatomic interaction, as well as in the external trap potential. Hopefully, this work will contribute towards making eigenvector continuation of great use within the field of *ultracold atoms*.

References

[1] D. Frame, R. He, I. Ipsen, L. Daniel, D. Lee, and E. Rrapaj, "Eigenvector Continuation with Subspace Learning," *Physical Review Letters*, vol. 121, no. 3, 2018-06. DOI: 10.1103/physrevlett.121.032501. arXiv: 1711.07090v2 [nucl-th].

[2] S. König, A. Ekström, K. Hebeler, D. Lee, and A. Schwenk, "Eigenvector continuation as an efficient and accurate emulator for uncertainty quantification," *Physics Letters B*, vol. 810, p. 135 814, 2020-11. DOI: 10.1016/j.physletb.2020.135814.

[3] A. Ekström and G. Hagen, "Global sensitivity analysis of bulk properties of an atomic nucleus," *Physical Review Letters*, vol. 123, no. 25, 2019-12. DOI: 10.1103/physrevlett.123.252501. arXiv: 1910.02922 [nucl-th].

[4] S. Wesolowski, I. Svensson, A. Ekström, *et al.*, "Fast & rigorous constraints on chiral three-nucleon forces from few-body observables," 2021. arXiv: 2104.04441 [nucl-th].

[5] T. Busch, B. Englert, K. Rzażewski, and et al., "Two Cold Atoms in a Harmonic Trap," *Foundations of Physics*, vol. 28, no. 4, pp. 549–559, 1998. DOI: 10.1023/A:1018705520999.

[6] E. J. Lindgren, J. Rotureau, C. Forssén, A. G. Volosniev, and N. T. Zinner, "Fermionization of two-component few-fermion systems in a one-dimensional harmonic trap," *New Journal of Physics*, vol. 16, no. 6, p. 063 003, 2014-06. DOI: 10.1088/1367-2630/16/6/063003. arXiv: 1304.2992v3 [cond-mat.quant-gas].

[7] M. H. Palmgren, *Solving complex physics problems at lightning speed*, 2021-02. [Online]. Available: https://www.chalmers.se/en/departments/physics/news/Pages/Solving-complex-physics-problems-at-lightning-speed.aspx (visited on 2021-05-21).

[8] Nobel Media AB, *The nobel prize in physics 1997*, 2021. [Online]. Available: https://www.nobelprize.org/prizes/physics/1997/summary/ (visited on 2021-01-20).

[9] W. Ketterle and N. V. Druten, "Evaporative cooling of trapped atoms," in, ser. Advances In Atomic, Molecular, and Optical Physics, B. Bederson and H. Walther, Eds., vol. 37, Academic Press, 1996, pp. 181–236. DOI: 10.1016/S1049-250X(08)60101-9.

[10] M. H. Anderson, J. R. Ensher, M. R. Matthews, C. E. Wieman, and E. A. Cornell, "Observation of Bose-Einstein Condensation in a Dilute Atomic Vapor," *Science*, vol. 269, no. 5221, pp. 198–201, 1995. DOI: 10.1126/science.269.5221.198.

[11] Nobel Media AB, *The nobel prize in physics 2001*, 2021. [Online]. Available: https://www.nobelprize.org/prizes/physics/2001/summary/ (visited on 2021-01-20).

[12] C. Chin, R. Grimm, P. Julienne, and E. Tiesinga, "Feshbach resonances in ultracold gases," *Reviews of Modern Physics*, vol. 82, no. 2, pp. 1225–1286, 2010-04. DOI: 10.1103/revmodphys.82.1225.

[13] C. R. Harris, K. J. Millman, S. J. van der Walt, *et al.*, "Array programming with NumPy," *Nature*, vol. 585, no. 7825, pp. 357–362, 2020-09. DOI: 10.1038/s41586-020-2649-2.

[14] P. Virtanen, R. Gommers, T. E. Oliphant, *et al.*, "SciPy 1.0: Fundamental Algorithms for Scientific Computing in Python," *Nature Methods*, vol. 17, pp. 261–272, 2020. DOI: 10.1038/s41592-019-0686-2.

[15] J. Lindgren, "Fermionization in one-dimensional cold atom systems," MSc thesis, Department of Fundamental Physics, Chalmers University of Technology, Gothenburg, Sweden, 2013. [Online]. Available: https://hdl.handle.net/20.500.12380/180197.

[16] H. J. Metcalf, P. van der Straten, and P. van der Straten, *Laser Cooling and Trapping*. New York, NY, USA: Springer, 1999. DOI: 10.1007/978-1-4612-1470-0.

[17] K. B. Gubbels, D. B. M. Dickerscheid, and H. T. C. Stoof, "Dressed molecules in an optical lattice," *New Journal of Physics*, vol. 8, no. 8, pp. 151–151, 2006-08. DOI: 10.1088/1367-2630/8/8/151. arXiv: cond-mat/0605056v2 [cond-mat.stat-mech].

[18] E. Tiesinga, C. J. Williams, F. H. Mies, and P. S. Julienne, "Interacting atoms under strong quantum confinement," *Physical Review A*, vol. 61, p. 063 416, 6 2000-05. DOI: 10.1103/PhysRevA.61.063416.

[19] J. J. Sakurai and J. Napolitano, *Modern Quantum Mechanics*, 2nd ed. Cambridge, England: Cambridge University Press, 2017. DOI: 10.1017/9781108499996.

[20] G. B. Arfken, H. J. Weber, and F. E. Harris, *Mathematical Methods for Physicists: A Comprehensive Guide*, 7th ed. Cambridge, England: Cambridge University Press, 2012. DOI: 10.1016/C2009-0-30629-7.

[21] L. Råde and B. Westergren, *Mathematics Handbook: for Science and Engineering*, 5th ed. Lund, Sweden: Studentlitteratur AB, 2004.

[22] J. Wenzel, *Pybind11*, 2017. [Online]. Available: https://pybind11.readthedocs.io/en/stable/index.html (visited on 2021-06-08).

[23] A. Sarkar and D. Lee, "Convergence of eigenvector continuation," *Physical Review Letters*, vol. 126, no. 3, 2021-01. DOI: 10.1103/physrevlett.126.032501. arXiv: 2004.07651v2 [nucl-th].

[24] D. K. Frame, "Ab Initio Simulations of Light Nuclear Systems Using Eigenvector Continuation and Auxiliary Field Monte Carlo," Ph.D. dissertation, Michigan State University, East Lansing, Michigan, United States, 2019. arXiv: 1905.02782 [nucl-th].

[25] Y. Saad, R. Lehoucq, and D. Sorensen, "An introduction to iterative projection methods," in *Templates for the Solution of Algebraic Eigenvalue Problems*, ch. 3, pp. 37–44. DOI: 10.1137/1.9780898719581.ch3. eprint: https://epubs.siam.org/doi/pdf/10.1137/1.9780898719581.ch3.

[26] L. Piela, "Two fundamental approximate methods," in *Ideas of Quantum Chemistry*, 2nd ed. Amsterdam, Netherlands: Elsevier, 2007, ch. 5, pp. 195–216. DOI: https://doi.org/10.1016/B978-044452227-6/50006-5.

[27] R. B. Lehoucq, D. C. Sorensen, and C. Yang, *ARPACK Users' Guide: Solution of Large-Scale Eigenvalue Problems with Implicitly Restarted Arnoldi Methods*. Philadelphia, PA, USA: SIAM, 1998. DOI: 10.1137/1.9780898719628. eprint: https://epubs.siam.org/doi/pdf/10.1137/1.9780898719628.

[28] R. Lundmark, "Tunneling theory for few-body systems in one-dimensional traps," MSc thesis, Department of Fundamental Physics, Chalmers University of Technology, Gothenburg, Sweden, 2014. [Online]. Available: https://hdl.handle.net/20.500.12380/197684.

DEPARTMENT OF PHYSICS
CHALMERS UNIVERSITY OF TECHNOLOGY
Gothenburg, Sweden
www.chalmers.se

CHALMERS
UNIVERSITY OF TECHNOLOGY